COLLEGE OF ENGINEERING

VIRGINIA POLYTECHNIC INSTITUTE AND STATE UNIVERSITY

BLACKSBURG, VIRGINIA

VPI-E-80-9 March 1980

USE OF TWO-DIMENSIONAL TRANSMISSION PHOTOELASTIC MODELS TO STUDY STRESSES IN DOUBLE-LAP BOLTED JOINTS: LOAD TRANSFER AND STRESSES IN THE INNER LAP

by

Michael W. Hyer
Department of Engineering Science and Mechanics

Prepared for:
National Aeronautics and Space Administration
Grant No. NSG-1621, Donald J. Baker, Technical Monitor
Materials Division
Langley Research Center
Hampton, VA 23665

Abstract

This report describes the progress to date on a project aimed at determining the stress distribution in the inner lap of double-lap, double-bolt joints. The investigations are being done by using photoelastic models of the joint. The principal idea is to fabricate the inner lap of a photoelastic material and to use a photoelastically insensitive material for the two outer laps. With this set-up, polarized light transmitted through the stressed model will respond principally to the stressed inner lap. The report describes the model geometry, the procedures for making and testing the model, and test results from the first model.

Testing of the first model has indicated the appearance of a photoelastic isotropic point, on the model centerline, part way between the two bolt holes. It has been demonstrated the exact location of this isotropic point is directly related to the amount of load transferred to each bolt in the joint. This phenomenon will then allow a direct measure of load transfer characteristics in the joint. In addition to this work, description of a finite-difference scheme, which uses raw photoelastic data and an x-y grid pattern superimposed on the model, is presented. This approach is being used to determine the stress distribution across the width of the joint.

Acknowledgement

This work was supported by the National Aeronautics and Space Administration's Langley Research Center, Materials Division, under Grant NSG-1621. The technical monitor is Donald J. Baker.

Table of Contents

LIST OF FIGURES

LIST OF FIGURES (Cont.)

1 - Introduction

Photoelasticity has been used many times as an aid in design and analysis of structural components. There exist several classic texts on the subject [1,2] and these have been quoted time and time again. However, the use of photoelasticity as a tool for the analysis of stress is so viable an approach that periodically new texts [3,4] are written which recast the classic treatments, discuss new approaches, new equipment, new methods of data reduction, new materials, and new applications. In addition, hardly a text on the experimental analysis of stress is published which does not devote a section or more to the subject of photoelasticity [5,6]. One of the strong points of photoelasticity is the ability to accurately model many aspects of a structural component which otherwise would be the subject of simplifying assumptions when attempts are made to obtain answers from approximate numerical schemes. Another strong point is that photoelastic analysis is not an expensive approach. Expensive optical benches are available for photoelastic analysis but excellent qualitative answers and good quantitative answers can be obtained with inexpensive set-ups. For the problem at hand, the stress analysis of the inner lap of a two-bolt double-lapped joint, both cost and modeling ability were factors in proposing the use of photoelasticity. However, a much more important consideration was the fact that the photoelastic effect is much stronger in photoelastic model materials than it is in other transparent plastics, such as plexiglas, which have mechanical properties nearly the same as the model materials. Thus, it was proposed to fabricate double-lap, double-hole joints using plexiglas and photoelastic material. The outer laps were to be plexiglas and the inner lap the photoelastic material. With this set-up,

when the model is placed in a standard photoelastic polariscope and loaded, the resulting fringe patterns observed in the model can be attributed almost entirely to the stresses in the inner lap.

This report describes the progress to date on the project. A description of the model is presented and the model making technique is discussed. The testing procedure is outlined and results of testing the first model are included. An unexpected result was the appearance of photoelastic isotropic point in the model partway between the two bolt holes. At this time it is felt the location of this isotropic point will be a strong indicator of the percentage of the total joint load reacted by each bolt. This phenomenon is fully discussed. To determine the stresses at various points in the inner lap, a scheme was developed which uses the raw photoelastic fringe data in a finite-difference formulation of the plane stress equations. This development is outlined and the stress distribution at several locations in the model are presented.

2 - Details of Model Geometry

The polariscope being used for testing has columnating lenes 305 mm (12 in.) in diameter. In addition, the load frame available for loading the model can accomodate a model 1.2 m (48 in.) long. The most difficult portion of the model to analyze is the area around the bolt holes. The larger the diameter the bolt holes, the easier it is to analyze the stresses in those regions. In addition, certain geometries or dimensional proportions to the model were important. The model dimensions were to be compatible with the dimensions of a series of quasi-isotropic graphite-epoxy bolted joints tested in a previous study [7,8,9]. With these graphite-epoxy joints, the distance between bolt-hole centers was six bolt-hole diameters and the bolt holes were no less than three bolt-hole diameters from the end of the joint. Thus the model had to be roughly twelve bolt-hole diameters long. In addition, certain joint-width to bolt-hole diameter ratios were to be considered, specifically, four, six and eight. These geometric requirements and the size of polariscope lenses dictated the size of the largest model, that being a model with a width to hole-diameter ratio of eight. A final consideration in model design was the method of applying the tensile load to the joint. In actual joints in both the inner and outer lap, at some distance away from the two bolt holes, a uniform stress computed from the simple P/A formula most likely exists. It is the interruption of this uniform stress by the bolt holes which causes stress concentrations and thus weaknesses in the joint. When testing models of bolted joints, or the actual joint specimens, care must be taken to insure the load introduction is far away from the bolt holes so a somewhat uniform state of stress exists away from the holes. If this is not the case the stress

distribution associated with the load introduction could interact with the stress distribution associated with bolt holes themselves. With such a situation the stress distribution in the joint could be incorrectly assessed. To avoid introducing spurious stress distributions, specimens can be designed long enough so that the actual joint region takes up, say, the central third of the specimen, the outer third on either side of the joint region being used to allow a uniform state of stress to develop between the load introduction and the bolts. The long-specimen approach, though desirable, can be costly due both to material costs and to machining costs. Thus the approach taken here, mainly to avoid costly machining as opposed to excessive material usage, was to use long aluminum load-introduction doublers. The idea was to generate a uniform stress-state in the doublers and attach them to the joint model three or four hole diameters away from the bolt hole with many small shoulder bolts. With the small connectors, the uniform stress-state would suffer only a localized perturbation in the zone around the connectors.

Taking into account all of the aforementioned factors, the bolt-hole diameter was chosen to be 22.2 mm (0.875 in.). This first model was chosen to have a width to hole-diameter ratio of eight and thus was 177 mm (7 in.) wide. The hole centers were 133 mm (5.25 in) apart and the free ends of both the inner lap and outer laps were 66.7 mm (2.63 in.) from the center of the second hole. For both the inner and outer laps the distance from a row of small number eleven shoulder bolts to the center of the lead holes was 82.6 mm (3.25 in.). (In this discussion, lead-hole or lead-bolt in a particular lap refers to that hole which reacts the applied tensile load first. The term second hole refers to the other hole in tandem. Obviously the lead hole for the

inner lap is the second hole for the outer laps and vice-versa.) Figures 1 and 2 show the bolted-joint model. In these figures the outer laps are to the left while the inner lap is to the right. The external tensile load was transferred to each doubler through a single 12.7 mm (0.500 in.) diameter pin near the ends. A spacer machined to be the same thickness as the inner lap actually connected the outer laps to the doubler through a second set of shoulder bolts. The inner lap was 6.35 mm (0.250 in.) thick PSM-1, a polycarbonate material marketed by Photolastic, Inc. [10]. The outer laps were 3.18 mm (0.125 in.) thick sheets of Acrylite, an acrylic material produced by American Cyanamide [11]. The doublers were fabricated from 3.18 mm (0.125 in.) thick aluminum. Though not related to the photoelastic testing, from the manufacturers data, Young's moduli for the materials are taken to be 2.76 GPa (400000 psi) for the PSM-1 and 3.27 GPa tension and 2.96 GPa compression (475,000 psi tension, 430,000 psi compression) for the Acrylite. Poisson's ratio for each is about 0.38.

The most serious concern was in the modeling of an actual bolt. For the graphite-epoxy specimens, the steel aircraft quality bolts had a Young's modulus of about 3-4 times that of the joint material. The bolts were fitted with flat washers and were torqued to specific values, depending on the bolt diameter and thread pitch. This torquing induced a through-the-thickness normal stress under the washer. This normal stress, via Poisson's ratio, would add to or substract from the load-induced stresses in the plane of the joint. In addition, friction between the washer and the joint could affect the load transfer from the bolt to the hole. The tolerance of the bolt in the hole was also important. Thus there are many variables regarding the bolt and washer

which could affect joint behavior. To proceed with modeling of a joint the following philosophy was adapted. If a joint were going to fail in bearing, a through-the-thickness compression ahead of the bolt would most likely counter bearing failure. If joint were going to fail in net-section tension, a through-the-thickness compression produces an in-plane compression at the net-section which could again counter a tensile failure, through a prestressing effect. Finally, friction between the washer and joint material allows some of the bolt load to be reacted into the specimen through shear (between washer and surface of joint) and thus all the load is not reacted by the hole itself. All of these effects are felt to be conservative. In addition, in a graphite-epoxy joint there are curing and moisture-induced stresses, free-edge effects at the hole edge, and voids in the material, all of which affect load-carrying capacity. Thus, the bolts in the photoelastic model were represented simply by acrylic dowels machined to fit snugly into the holes. With dowels, as opposed to bolts, the through-the-thickness stresses were absent. However, because there was no nut, bolt-head or washers, viewing of the fringe pattern to the edge of the hole would be possible. Using acrylic dowels, Young's modulus of the bolt material was the same as Young's modulus of the joint material, different than the three or four to one ratio in the graphite-epoxy joints. However, Jessop, Snell and Holister [12] saw no appreciable difference in peak stresses for bolt-to-joint modulus ratios of from 1:1 to 30:1. Thus the use of acrylic for the dowels, as opposed to a stiffer material, was not felt to be a problem. These dowels are shown in Fig. 2.

3 - Details of the Model Making

The major concerns with actually making the model were: (1), maintaining accurate tolerances of the specified dimensions; (2), insuring accurate alignment of the two bolt holes along the model centerline; (3), insuring identical hole placement and hole diameter in all three laps and; (4), minimizing heat-induced machining stresses.

After much consideration, it was decided to machine all three pieces simultaneously, as a sandwich. The major effect of this was to insure alignment of the bolt holes. In addition, to minimize the machining stresses around the two bolt holes, the holes were machined while the three layers were submerged in a coolant. To begin the machining of the joining the three laps were clamped together and the long sides machined parallel to each other. Then the rows of number eleven holes were drilled in the clamped sandwich, perpendicular to the edges. A flat, open, tray-like tank was fabricated and mounted on a milling machine and the three layers placed in it. Precision steel pins protruding from the bottom of the tank were used with the number eleven holes to maintain the original alignment of the three laps. The laps were again clamped lightly together and the tray filled with coolant. The two bolts holes were then machined with an off-set cutter.

This machining procedure has proven satisfactory and will be used in the future. With this first model, however, the milling tool caught the edge of the PSM-1 resulting in a chip and a residual stress near the row of number eleven bolts. The stress is localized and quite noticable when the model is viewed in a polariscope but its effects do not extend more than 25-28 mm (1.00-1.50 in.) beyond the edge.

The aluminum doublers were machined in standard fashion. Again the edges were machined parallel and the row of number eleven holes drilled. Using the number eleven holes as a reference, the 12.7 mm (0.500 in.) diameter loading holes were drilled. It was critical that the 12.7 mm (0.500 in.) loading holes and the model bolt holes all be in a straight line. If not, the model would be subjected to unwanted moments. Using the number eleven holes in all parts of the model as a reference hopefully minimized any undesirable moments.

The coolant used throughout the machining operation was a water-soluble coolant.

4 - Testing Procedure

4.1 - Test Set-Up

For testing, the model was placed vertically in the loading frame. Figure 3 shows a picture of the loading frame with the model in place. The loading frame is mounted on a rolling bed so that it can be moved in and out of the polariscope easily. Figure 4 shows a closer view of the model and the loading frame in position in the polariscope. Visible in both illustrations is the load cell (cylindrical object, above specimen, with wire coming from it) used to monitor the total axial load applied to the model. A variety of pinned connections along the load train insure that only axial forces are transmitted to the model. The tensile load is applied by a screw-mechanism at the top of the load frame.

The polariscope itself has a 250-watt mercury-vapor light source. The columnating lenses, the polarizer, analyzer and quarter-wave plates are all housed in the black framework on either side of the opening for the loading frame. Figure 4 shows some detail of these components.

4.2 - Fringe Patterns and the Appearance of an Isotropic Point

Figure 5 shows the inner lap as viewed with the polariscope in the lightfield circular configuration. The acrylic dowels are not in place nor is there any load on the lap. As can be seen the model is generally free of machining stresses. There is a slight darkening at the top of the upper hole and this darkened area extends away from hole toward the upper right. This is felt to be due to a combination of a slight amount of residual machining stress around the bolt hole and stresses induced by not having perfect alignment of all of the number eleven

holes in the stiff aluminum doublers and the soft PSM-1. Visible on the model are a horizontal grid system, just below the top hole, and a vertical scale along the model centerline. The horizontal grid is used for finite-difference computation of the stress distribution across the width of the specimen. The vertical scale is used to determine the exact vertical location of a particular zeroth-order fringe. Use of the grid and scale will be discussed.

Figure 6 shows the isochromatic fringe pattern for the dark field circular polariscope setting. The load is 2.20 kN (500 lb.). In this illustration the view is through the two acrylic outer layers and the one inner layer of PSM-1. It is safe to say the stress level in each outer lap is quite close to the stress level in the inner lap. Each outer lap supports one-half the load the inner lap carries but each outer lap is only one-half as thick as the inner lap. Figure 7 shows the isochromatic fringe pattern of an Acrylite disk and a PSM-1 disk, each subjected to identical diametrical compressive loads. It is obvious the PSM-1 is much more sensitive to the photoelastic effect and so the fringes of Fig. 6 can be attributed almost exclusively to the stresses in the inner lap.

The fringe count in Fig. 6 can be easily identified, particularly when the fringes are generated with white light. The lower right and left corners of the model are stress-free (since they are convex free corners) and the difference in principal stresses is zero. Thus even in white light the corners are black, this being identified with zeroth fringe. As one proceeds to the interior of the model the fringe count goes up in integer fashion. All fringes except the zeroth order are essentially bands of various colors. Thus each time a colored band is

crossed (dark band in the figure) the fringe count changes by one. Though not apparent in the black and white tones of Fig. 6, when the image shown in Fig. 6 was first seen it was with white light and an unusual feature was immediately apparent. The small solid dark spot on the centerline, about one-half the distance between the holes, was actually black. Except for the corners and this spot, all fringes were colored. This black spot (a fringe of order zero), when seen in photoelastic models indicates either an isotropic point or a singular point. These are explained briefly below.

The photoelastic effect, as being used in this study, measures the difference in the numerical value of the principal stresses. The number of fringes times a calibration constant gives the numerical value of the differences in principal stresses, i.e.,

$$\sigma_1 - \sigma_2 = cN, \tag{1}$$

c being the calibration constant in Pa/fringe (psi/fringe) and N being the fringe order. The fringe order being zero implies

$$\sigma_1 - \sigma_2 = 0, \tag{2}$$

which requires either

$$\sigma_1 = \sigma_2 = 0 \tag{3}$$

or

$$\sigma_1 = \sigma_2 = ?. \tag{4}$$

The former case is refered to as a singular point, that is, both principal stresses are zero. This can occur on the boundary or in the interior of the model. The second case is referred to as an isotropic point, so-called because the principal stresses, though unknown, are equal. At an isotropic point a state of hydrostatic-like stress exists.

With a hydrostatic-like stress, the stresses being either tensile or compressive, the stresses are the same in all directions and hence the term isotropic.

4.3 - Load-Transfer Hypothesis

It was hypothesised that the vertical location of the isotropic point, relative to the distance between the hole centers, depended on the percentage of the total load reacted by each bolt. The problem of determining the transfer of the total load to the two bolts is statically indeterminant and the elasticity of the inner and outer laps must be considered in any attempt to determine the amount of load reacted by each bolt. If the hypothesis were true, the isotropic point location would be a very convenient way to assess load transfer. Taking the hypothesis one step further, if this isotropic point exists for all two-bolt joints, then the effect of joint width, hole diameter, distance between bolts, distance of the second bolt to the end of the lap, and other geometrical changes could be assessed in relation to load transfer, at least for these isotropic joints. The implications of the isotropic point for quasi-isotropic joints is an even further extrapolation of the hypothesis.

To test the original hypothesis for this first model the outer laps were removed and a scheme to load each bolt independently was devised. The plexiglas dowels were inserted into the holes of the inner lap and a hanger, utilizing dead weights and attached to the bottom dowel, was used to load the bottom hole a known amount. The loading-screw mechanism at the top of the load frame actually translated the model up and down

as the screw was rotated. A flexible braided-wire harness was fixed to the sides of the load frame and looped over the top dowel. As the model was translated up by the loading screw the harness loaded the top hole while the dead weights loaded the bottom hole. The load cell registered the total load and knowing the dead-weight load on the bottom hole, the load on the top hole could be computed. To help locate the isotropic point on the model, a grid, marked to a resolution of 2.54 mm (0.1 in), was scribed on the model centerline. This is the vertical scale visible in Fig. 5. Figure 8 shows the set-up for loading each hole independently.

With the ability to vary each hole load independently, the vertical location of the isotropic point was determined for a variety of load conditions. Its location vs. bolt loading was determined for low and high total load levels; for constant total load and variable upper and lower bolt loads; for constant lower bolt load and variable upper and total bolt loads; interchanging the two dowels; and various other conditions. In each case, the location of the isotropic point had the same very specific relation to the percentage of load reacted by each bolt. Figure 9 shows the movement of the isotropic point as a function of hole loading. It is clear the percentage of load on each hole affects the position of the isotropic point. Figure 10 presents experimental data for some of the many conditions tested. Plotted on the vertical axis is the nondimensionalized distance of the isotropic point, C, from the center of the top hole. The horizontal axis represents the proportion of total load, T, reacted by the lead (top) hole, P_1. The data from all conditions cluster tightly about a relationship which appears to be slightly nonlinear. The nonlinearity is felt to be due to the

change in contact area of the bolt in the hole as the load level in each hole changes. This is a geometric nonlinearity.

Thus as shown in Fig. 11, with the plexiglas laps back in place, having run a series of experiments tc produce a curve as in Fig. 10, the location of the isotropic point can be observed. Working backwards, the percentage of load reacted by each hole can be determined. From Fig. 6 C = 61.9 mm (2.44 in.) and using the value of E of 133 mm (5.25 in.), C/E = 0.465. From the data of Fig. 10 the first bolt of this model reacts about 56% of the load, transfering 44% to the second bolt.

During the next six months of the grant work models with varying widths will be constructed to determine if the isotropic point phenomenon exists for other geometries. If it does, the effect of joint width-to-hole diameter on load transfer will be assessed by this method.

5 - Stress Distribution in the Joint

5.1 - Extent of Information from Photoelastic Data

Besides knowing the percentage of the total load reacted by each bolt, it is desirable to know the stresses at various locations in the model. Specifically, stresses along the joint centerline, stresses at the hole edges, and stresses across a widthwise section are all of interest. Since this is a plane-stress problem this is tanamount to knowing σ_x, σ_y, and τ_{xy} at each location on the joint, the subscripts x and y reflecting some global or local orthogonal coordinate system. The polariscope being used in the experiment indicates, at every point in the model by way of fringes, two quantities related to the stress at that point: (1), the difference in principal stresses (mentioned earlier) $\sigma_1 - \sigma_2$, and; (2), the orientation of the principal stresses, θ, with respect to, say, the widthwise (x - in this report) or centerline (y -in this report) directions. In photoelastic work the angle θ is referred to as the isoclinic parameter or the isocline angle. However, it is just the principal stress direction relative to the axis of polarization of the light incident on the model. In the cases discussed here this axis is the horizontal (widthwise, x) axis.

Referring to Fig. 12, the known stresses in the x-y system, σ_x, σ_y, and τ_{xy}, can be used to determine the stress in an x'-y' system; a system rotated counterclockwise an angle ϕ from the x-y system. This can be accomplished by the well-known transformation equations. These equations are:

$$\sigma_x' = \left(\frac{\sigma_x + \sigma_y}{2}\right) + \left(\frac{\sigma_x - \sigma_y}{2}\right)\cos(2\phi) + \tau_{xy}\sin(2\phi), \tag{5}$$

$$\sigma_y' = \left(\frac{\sigma_x + \sigma_y}{2}\right) - \left(\frac{\sigma_x - \sigma_y}{2}\right)\cos(2\phi) - \tau_{xy}\sin(2\phi), \tag{6}$$

$$\tau_{xy}' = -\left(\frac{\sigma_x - \sigma_y}{2}\right)\sin(2\phi) + \tau_{xy}\cos(2\phi). \tag{7}$$

On the other hand, the stresses in the x-y system can be determined from the stresses in the x'-y' system by inversion of eqs. (5)-(7). This operation leads to

$$\sigma_x = \left(\frac{\sigma_x' + \sigma_y'}{2}\right) + \left(\frac{\sigma_x' - \sigma_y'}{2}\right)\cos(2\phi) - \tau_{xy}'\sin(2\phi), \tag{8}$$

$$\sigma_y = \left(\frac{\sigma_x' + \sigma_y'}{2}\right) - \left(\frac{\sigma_x' - \sigma_y'}{2}\right)\cos(2\phi) + \tau_{xy}'\sin(2\phi), \tag{9}$$

$$\tau_{xy} = \left(\frac{\sigma_x' - \sigma_y'}{2}\right)\sin(2\phi) + \tau_{xy}'\cos(2\phi). \tag{10}$$

If the primed system is the principal stress system and σ_x' is assigned to σ_1 and σ_y' is assigned to σ_2, then since $\tau_{xy}' = \tau_{12} = 0$ and $\phi = \theta$, eqs. (8)-(10) become

$$\sigma_x = \left(\frac{\sigma_1 + \sigma_2}{2}\right) + \left(\frac{\sigma_1 - \sigma_2}{2}\right)\cos(2\phi), \tag{11}$$

$$\sigma_y = \left(\frac{\sigma_1 + \sigma_2}{2}\right) - \left(\frac{\sigma_1 - \sigma_2}{2}\right)\cos(2\phi), \tag{12}$$

$$\tau_{xy} = \left(\frac{\sigma_1 - \sigma_2}{2}\right)\sin(2\phi). \tag{13}$$

(note: θ is still measured positive counterclockwise from the + x-axis.) The convention used herein is to assign σ_1 to the algebraically larger principal stress. If we knew $(\sigma_1 + \sigma_2)$, $(\sigma_1 - \sigma_2)$, and θ at each point in the model, σ_x, σ_y, and τ_{xy} would be known at each point in the model through eqs. (11)-(13). Since photoelastic information gives only $(\sigma_1 - \sigma_2)$ and θ, we need a third relation or measurement to deter-

mine all the stresses. Subtracting eq. (12) from eq. (11) and using the nomenclature of eq. (1) results in

$$(\sigma_x - \sigma_y) = cN\cos(2\theta), \tag{14}$$

$$\tau_{xy} = \frac{cN}{2}\sin(2\theta). \tag{15}$$

Thus with the isochromatic fringe count N and the isocline θ at each point, τ_{xy} can be determined directly at each point. However, as opposed to knowing σ_x and σ_y individually, N and θ only allow determination of the differences in σ_x and σ_y.

Determining σ_x and σ_y (referred to as separation of stresses) can be accomplished several ways. One way is knowing that σ_x, σ_y, and τ_{xy} satisfy the differential equilibrium equations of plane stress, namely

$$\frac{\partial\sigma_x}{\partial x} + \frac{\partial\tau_{xy}}{\partial y} = 0, \tag{16}$$

$$\frac{\partial\tau_{xy}}{\partial x} + \frac{\partial\sigma_y}{\partial y} = 0. \tag{17}$$

The method chosen to determine σ_x, σ_y, and τ_{xy} is to use eqs. (14), (15) and finite-difference representations of eqs. (16) and (17).

5.2 - Finite-Difference Representation of the Plane Stress Equilibrium Equations

Consider a rectangular array of points in an x-y coordinate system, Fig. 13. For point $(i, j + \frac{1}{2})$, point a in Fig. 13, the following approximation can be written,

$$\left(\frac{\partial\sigma_x}{\partial x}\right)_{i,j+\frac{1}{2}} = \frac{1}{\Delta x}\{(\sigma_x)_{i,j+1} - (\sigma_x)_{i,j}\} \tag{18}$$

Also, to complement eq. (18),

$$\frac{\partial \tau_{xy}}{\partial y}_{i,j+\frac{1}{2}} = \frac{1}{2}\left\{\left(\frac{\partial \tau_{xy}}{\partial y}\right)_{i,j+1} + \left(\frac{\partial \tau_{xy}}{\partial y}\right)_{i,j}\right\} \tag{19}$$

where

$$\frac{\partial \tau_{xy}}{\partial y}_{i,j+1} = \frac{1}{2\Delta y}\{(\tau_{xy})_{i+1,j+1} - (\tau_{xy})_{i-1,j+1}\} \tag{20}$$

and

$$\frac{\partial \tau_{xy}}{\partial y}_{i,j} = \frac{1}{2\Delta y}\{(\tau_{xy})_{i+1,j} - (\tau_{xy})_{i-1,j}\} \tag{21}$$

Equation (16) now becomes

$$(\sigma_x)_{i,j+1} - (\sigma_x)_{i,j} + \frac{\Delta x}{4\Delta y}\{(\tau_{xy})_{i+1,j} - (\tau_{xy})_{i-1,j}\} +$$

$$\frac{\Delta x}{4\Delta y}\{(\tau_{xy})_{i+1,j+1} - (\tau_{xy})_{i-1,j+1}\} = 0. \tag{22}$$

Equation (22) is a approximation to the equilibrium conditions at specific discrete points along row i.

For point $(i + \frac{1}{2}, j)$, point b in Fig. 13, the following approximations may be written:

$$\frac{\partial \sigma_y}{\partial y}_{i+\frac{1}{2},j} = \frac{1}{\Delta y}\{(\sigma_y)_{i+1,j} - (\sigma_y)_{i,j}\}, \tag{23}$$

and

$$\frac{\partial \tau_{xy}}{\partial x}_{i+\frac{1}{2},j} = \frac{1}{2}\left\{\left(\frac{\partial \tau_{xy}}{\partial x}\right)_{i+1,j} + \left(\frac{\partial \tau_{xy}}{\partial x}\right)_{i,j}\right\}, \tag{24}$$

with

$$\frac{\partial \tau_{xy}}{\partial x}_{i+1,j} = \frac{1}{2\Delta x}\{(\tau_{xy})_{i+1,j+1} - (\tau_{xy})_{i+1,j-1}\} \tag{25}$$

and

$$\frac{\partial \tau_{xy}}{\partial x}_{i,j} = \frac{1}{2\Delta x}\{(\tau_{xy})_{i,j+1} - (\tau_{xy})_{i,j-1}\}. \tag{26}$$

Thus, eq. (17) has the approximate representation at point b of

$$(\sigma_y)_{i+1,j} - (\sigma_y)_{i,j} + \frac{\Delta y}{4\Delta x}\{(\tau_{xy})_{i+1,J+1} - (\tau_{xy})_{i+1,j-1}\} +$$

$$\frac{\Delta y}{4\Delta x}\{(\tau_{xy})_{i,j+1} - (\tau_{xy})_{i,j-1}\} = 0. \qquad (27)$$

Equation (27) can be applied at discrete points along row $(i + \frac{1}{2})$, points b, and at discrete points along row $(i - \frac{1}{2})$, points b'.

The particular finite-difference kernels presented here are somewhat different than normal in that equilibrium in the x-direction, eq. (15), is satisfied at one set of points, a and a', and equilibrium in the y-direction, eq. (17), is satisfied at a different set of points, b and b'. However refering to Fig. 13, the central point, point (i,j), is surrounded with equilibrium requirements and photoelastic data from all nine points is used in the formulation. The conventional central-difference representation of equilibrium at point i,j would only use information from points (i+1,j), (i-1,j), (i,j+1) and (i,j-1). In fact photoelastic data from the point at which you were trying to find the stresses would not even enter into the calculations. Berghaus [13] used a similar scheme in an overdetermined equilibrium approach where he purposely wrote more equations than necessary and satisfied them in a least-squares sense. The idea was adapted for this bolted-joint problem.

Referring to Fig. 5, the finite-difference scheme was applied to horizontal grid systems scribed onto the model. Scribing the grid onto the model was more desirable than superimposing a grid system over the model image. The superposition could have been accomplished by placing a transparent screen, with the grid system on it, in the light path of the polariscope. Alternately it could have been done photographicall

when pictures of the fringe patterns were printed. With the method chosen here, slippage of the grid relative to the model was not a problem and since a photographic stage was not necessary, fringe data vs. x-y location could be taken in real time during the testing.

Although the photographs show only one grid system, three grids were scribed on the model at the positions shown in Fig. 14. Results for all three grid systems will be presented. First the complete scheme for determining the stresses, starting with the raw fringe data and ending with the three stresses at each point in the grid, is described.

The equations used for determining the stresses are summarized and rewritten slightly as follows:

$$(\sigma_x)_{i,j} - (\sigma_y)_{i,j} = cN_{i,j}\cos(2\theta_{i,j}) \tag{28}$$

$$(\tau_{xy})_{i,j} = \frac{c}{2} N_{i,j}\sin(2\theta_{i,j}) \tag{29}$$

$$(\sigma_x)_{i,j+1} - (\sigma_x)_{i,j} + \frac{\Delta x}{4\Delta y}\{(\tau_{xy})_{i+1,j} - (\tau_{xy})_{i-1,j}\} + \frac{\Delta x}{4\Delta y}\{(\tau_{xy})_{i+1,j+1} - (\tau_{xy})_{i-1,j+1}\} = 0 \tag{22}$$

$$(\sigma_y)_{i+1,j} - (\sigma_y)_{i,j} + \frac{\Delta y}{4\Delta x}\{(\tau_{xy})_{i+1,j+1} - (\tau_{xy})_{i+1,j-1}\} + \frac{\Delta y}{4\Delta x}\{(\tau_{xy})_{i,j+1} - (\tau_{xy})_{i,j-1}\} = 0. \tag{27}$$

In addition, at the left and right free-edges of the model,

$$\sigma_x = 0, \ \tau_{xy} = 0. \tag{30}$$

The quantity $N_{i,j}$ refers to the isochromatic fringe order at point i,j and $\theta_{i,j}$ refers to the value of the isoclinic angle of point i,j.

Equations (28), (29), (22), (27) and eq. (30), eq. 30 being applied to the six grid points on the boundary, give the stresses at each grid point location. As seen in Fig. 5, for each grid there are 29 x 3

points, resulting in 261 unknown stresses. Rather than eliminate unknowns by using eq. 30 at the appropriate points, equations of this type are just considered as twelve of the 261 required equations.

To impliment the solution, the isochromatic fringe order, $N_{i,j}$, and the isocline angle, $\theta_{i,j}$, are required at each grid point. The grid system used a Δx of 6.35 mm (0.25 in.) and a Δy of 5.08 mm (0.20 in.). To determine $N_{i,j}$ at each point the x-location of the integer and 1/2-order fringes along each of the three horizontal lines was determined, in real time, by projecting the model image through translucent paper. Using the known distance between vertical grid lines, the horizontal position of each fringe was determined directly from the image. Thus for example, referring to Fig. 6, for the middle of the three grid lines, fringe 1 (N=1) intersects the line 41.3 mm (1.625 in.) from the left edge and about the same distance from the right edge. Fringe 2 (N=2) intersects the top line 38.1 mm (1.5 in.) from the left edge and the same distance from the right edge. For the top line, fringe 3 intersects it 59.0 (2.32 in.) from the left edge and about the same distance from the right edge. A good approximation to the exact fringe location can be determined by observing the image of the fringes directly in the polariscope. The photograph of Fig. 6 is not a good indication of the fringe sharpness actually observed. Considerable resolution was lost printing the photographs for this report.

Knowing integer and 1/2-order fringes values vs. x, the fringe order at any given x is determined by interpolation between points. The fringe order at the edges and centerline of the model were determined by Tardy compensation. Cubic splines were used to generate the interpolated functional relation of N vs. x for each of the three horizontal

lines. Figure 15 shows the fringe relation for the grid system shown in Fig. 5, grid 1. The figure shows both the spline interpolation and the original integer and 1/2-order fringe information for all three horizontal lines of the grid. At present, simple cubic splines are used to generate the N vs. x relation. In the future, smoothed cubic splines will be used. Smoothed splines allow a weighting factor to be assigned to each experimental data point and allow a smoothing parameter to be specified. For regions in the model which have a low stress gradient, such as at the model's edges, the fringes are wide. Locating the exact center of the fringe is not as precise a process as locating the centers of the sharply defined fringes. With weighting factors assigned to the various fringe orders, the wider fringes can be assigned weights of, for example, 0.9 while the sharp fringes can be assigned weights of unity or more. The smoothing parameter can be used to allow some uncertainty as to how accurately, overall, the x-location of the integer and 1/2-order fringes can be determined. It is felt the x-location can only be resolved, for example, to one part in 10, the smoothing factor can be chosen to allow for this. Thus, using the weighting factors and the smoothing parameter, the extrapolated curve does not have to pass through all the original integer and 1/2-order data points, as it does in Fig. 15.

The isoclinic angle as a function of x is determined in an identical manner. Figure 16 shows the variation of θ with x. The physical interpertation of the variation of isocline angle with x is quite straightforward. In the format presented here the isocline angle is the angle the algebraically larger principal stress, σ_1, makes with respect to the

horizontal, x, axis. At the edges of the model $\sigma_x = \tau_{xy} = 0$ and σ_y is a tensile value. At those locations, $\sigma_y = \sigma_1$, the algebraically larger principal stress; hence $\theta = \pm 90°$. On the centerline $\tau_{xy} = 0$ and σ_y is a large compressive value. The stress σ_x is smaller in absolute value than σ_y and so, regardless of whether it is a tension or compression, it is the algebraically larger principal stress. There $\sigma_x = \sigma_1$ and $\theta = 0$. The isocline angle θ is antisymmetric with x, reflecting the antisymmetry of τ_{xy} (refer to eq. (29)).

Close examination of Fig. 16 indicates the isocline angles are not exactly $\pm 90°$ at the right and left edges. Theoretically at the free edges the isocline angle from all three horizontal grid lines are equal and equal to $\pm 90°$. The deviation from the ideal in the experiment is due to accurately defining the center of the isoclinic fringe in areas where it does not vary much spatially. In addition, smaller errors in the exact alignment of polarizing axes of the optical elements can lead errors of the magnitude shown. It is just about impossible to eliminate these two types of errors. However, smoothing and weighting of the experimental data can compensate for these problems.

The procedure for measuring the isoclinics was slightly different than the procedure for measuring the isochromatics. The plexiglas, while not affecting the isochromatic fringe order, does disturb the isoclinic measurement. Therefore, once the location of the isotropic point was determined, the model was loaded as in Fig. 8, without the outer laps, to reproduce the same isotropic point location. The isoclinic measurements were taken from the dead-weight loaded model. Typical isoclinic fringes are shown in Figs. 17 and 18. The physical

interpretation of the isoclinic fringe is as follows. For a given isoclinic value, say $\theta = 45°$ as in Fig. 18, the fringe is the locus of points where the σ_1 principal stress direction makes an angle at 45° with the horizontal. Figure 19 illustrates the idea. Referring to Fig. 18, the 45° isocline intersects the bottom line of the horizontal grid roughly 15.9 mm (0.625 in.) on either side of the specimen centerline. Since an isotropic point is a point of hydrostatic-like stress, all directions are principal stress directions. Thus all isoclines pass through the isotropic point. Figures 17 and 18 show this. It should be mentioned that with certain polariscopic arrangements only the isochromatic fringes appear, as in Fig. 6. With other optical element arrangements both the isoclinic and isochromiatic fringes appear. In addition, the isochromatic fringes tend to wash out the isoclinic fringes. Thus when measuring the isoclinic angle it is sometime necessary to adjust the level of the load to move certain isochromatic fringes, the location of which are functions of load level. This is done so that the location of a washed out isoclinic fringe, the location of which is not a function of load level, can be determined. Therefore the load levels in Fig. 6 and 17 and 18 are not the same but the proportion of total load to each hole is the same.

Because of the degree of symmetry and antisymmetry displayed by N and θ vs. x, it was decided to use the finite-difference scheme on just one-half the model, i.e., to the right of the centerline. Thus the data for N and θ on the right and left side of the centerline was averaged and the analysis was assumed symmetric. This decreased by a factor of two the amount of data reduction. For this first run through the analysis scheme this was not felt to be a major restriction, particularly in light

of the aforementioned regularity of N and θ with x.

5.3 - Stress Distribution at Grid 1

Figure 20 shows the σ_y stresses along the three horizontal grid lines for grid 1. The stresses have been nondimensionalized by the gross-section stress ahead of the lead bolt. The gross-section stress is the total applied load, T, divided by the gross-section area, 178 mm x 6.35 mm = 1130 mm^2 (7 in x 0.25 in = 1.75 in^2). The σ_y stresses are compressive near the centerline and tensile over the remaining width. Obviously, on the centerline, the compressive stresses increase approaching the hole edge. The net-force determined by integrating σ_y across the center of the three lines, using simply the trapezoidal rule, is 828 N (186 lb.), or 37% of the total applied load of 2.22 kN (500 lb.). The isotropic point location predicts this load to be 44%. This difference represents 17% of the average of the two predictions. In theory, the stress on the center line of the three grid lines is the most accurate because it is only for this line that the central-difference derivative approximation exists. These numbers are commented on later.

Figure 21 shows the σ_x stresses along the three grid lines while Fig. 22 shows τ_{xy}. These stresses also have been nondimensionalized by the gross-section stress. The positive values of σ_x near the centerline indicate the bolt is trying to split the joint along the centerline. This behavior can be explained as follows. Along the joint centerline the bolt pushes downward on the hole edge. To either side of the centerline but still on the bottom of the hole, the bolt pushes on the hole edge with a large force. However the forces are inclined to the left and right. It is the horizontal components of the inclined forces which tend to split the joint, in tension, along the centerline below the hole. The shear stress behavior is not at all unexpected.

5.4 - Stress Dimension at Grid 2

Figure 23 and 24 show the isochromatic fringe order and the isocline angle for the three lines of grid 2. For the sake of comparison the scales on the figures for N and θ are the same for grids 1, 2 and 3. As can be seen, there is relatively little variation of fringe order or isocline angle with width. It appears that at this distance away from the lead hole the stresses have become much more uniform. The nearly 90° value of the isocline across the width means the tensile y-directed stress is close to being equal to the largest principal stress. Coupling this information with the nearly constant fringe order, it can be predicted σ_y is practically constant with x of the this location.

Figure 25 shows the variation at σ_y with x as computed from the photoelastic data. That σ_y is nearly constant is shown in this figure. Figures 26 and 27 show σ_x and τ_{xy}. The net force, determined by integrating σ_y across the width with the trapazoidal rule is computed to be 983 N (221 lb.) or 44% of the total load, the same as predicted by this isotropic point location.

5.5 - Stress Distribution at Grid 3

Figures 28 and 29 show the isochromatic fringe order and the isocline angle for the three lines of grid 3. The variation of these quantities with the widthwise coordinate is similar to the characteristics of grid 1. The main difference between grid 3 and grid 1 is that there should be no net y-direction force at grid 3. Figures 30-32 show the variations of σ_y, σ_x, and τ_{xy} with joint width. As expected, all three stresses asymptotically approach zero toward the edge. Using the trapezoidal rule on the σ_y stress, the net-force in the y-direction is computed to be 37.0 N (8.32 lb), not a serious force imbalance.

6 - Discussion

Using the trapezoidal rule for integration is not felt to be the best approach. In the future, the computed stress will be connected with a cubic spline, perhaps smoothed, and the area under this used to compute net-force in the y-direction. It is felt that the trapezoidal rule works well for the σ_y stress of grid 2 but when the stress changes abruptly with x the straight-line approximation of the trapezoidal rule is too crude. In addition now that it is known where the stresses vary the most, the finite-difference mesh can be made nonuniform to perhaps increase the accuracy. Although not felt to be a problem, insteady of averaging the data from the left side and right side of the model, computation across the entire width will be considered in the future. With this approach any bending effects can be determined.

In conclusion, between the isotropic point location and integration of the σ_y stresses, a good indication of load distribution to the two bolts can be determined. If the isotropic point does not occur for other model geometries, the σ_y integration method can be used.

References

1. Coker, E. G. and Filon, L. N. G., A Treatise on Photo-elasticity, Cambridge at the University Press (1957) (revised by H. T. Jessop).

2. Frocht, M. M., Photoelasticity, Vols. 1 and 2, John Wiley and Sons, Inc., New York, (1941).

3. Kuske, A. and Robertson, G., Photoelastic Stress Analysis, John Wiley and Sons, New York, New York, (1974).

4. Aben, H., Integrated Photoelasticity, McGraw-Hill, Inc., New York, New York, (1979).

5. Dalley, J. W. and Riley, W. F., Experimental Stress Analysis 2nd Edition, McGraw-Hill, New York, (1978).

6. Budynas, R. G., Advanced Strength and Applied Stress Analysis, McGraw-Hill, Inc., New York, New York, (1977).

7. Hyer, M. W. and Lightfoot, M. C. Composite Bolted Joint Specimens: Experimental Results, NASA CR-158964 (1978).

8. Hyer, M. W. and Lightfoot, M. C., Ultimate Strength of High-Load Capacity Composite Bolted Joints, ASTM STP-674 Composite Materials: Testing and Design, 5th Conference, 118-136 (1979).

9. Hyer, M. W., Perry, J. C., Lightfoot, M. C., Load Transfer in Composite Bolted Joints, AIAA Paper No. 80-0779 (1980).

10. Measurements Group, Photolastic, Inc., P.O. Box 27777 Rayleigh, NC 27611.

11. American Cyanamide, Wayne, NJ 07470.

12. Jessop, H. T., Snell, C. and Hollister, G. S., Photoelastic Investigation in Connection with the Fatigue Strength of Bolted Joints, The Aeronautical Quarterly, August 1955, p. 230-239.

13. Berghaus, D. G., Overdetermined Photoelastic Solutions Using Least-Squares, Exp. Mech. Vol. 13, No. 3, 97-104 (1973).

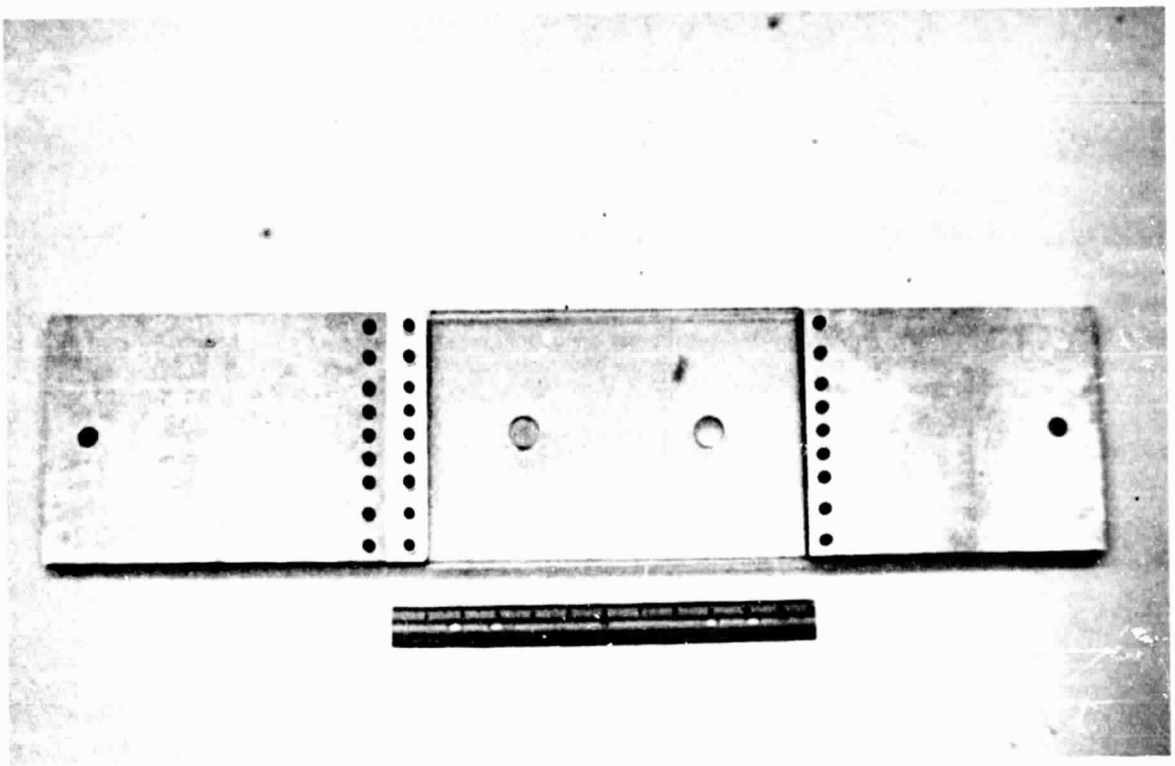

Fig. 1 - Joint Model

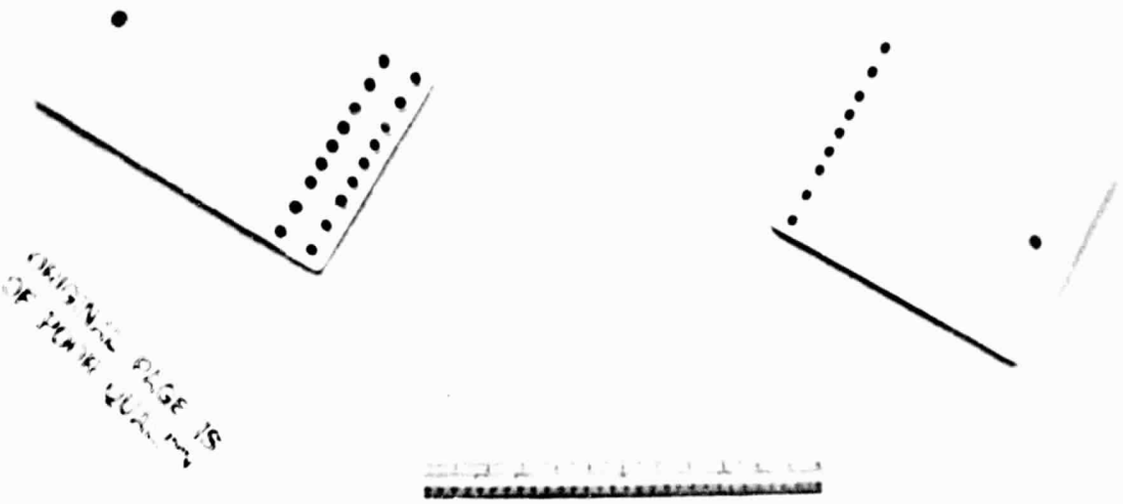

Fig. 2 - Joint Model, Individual Components

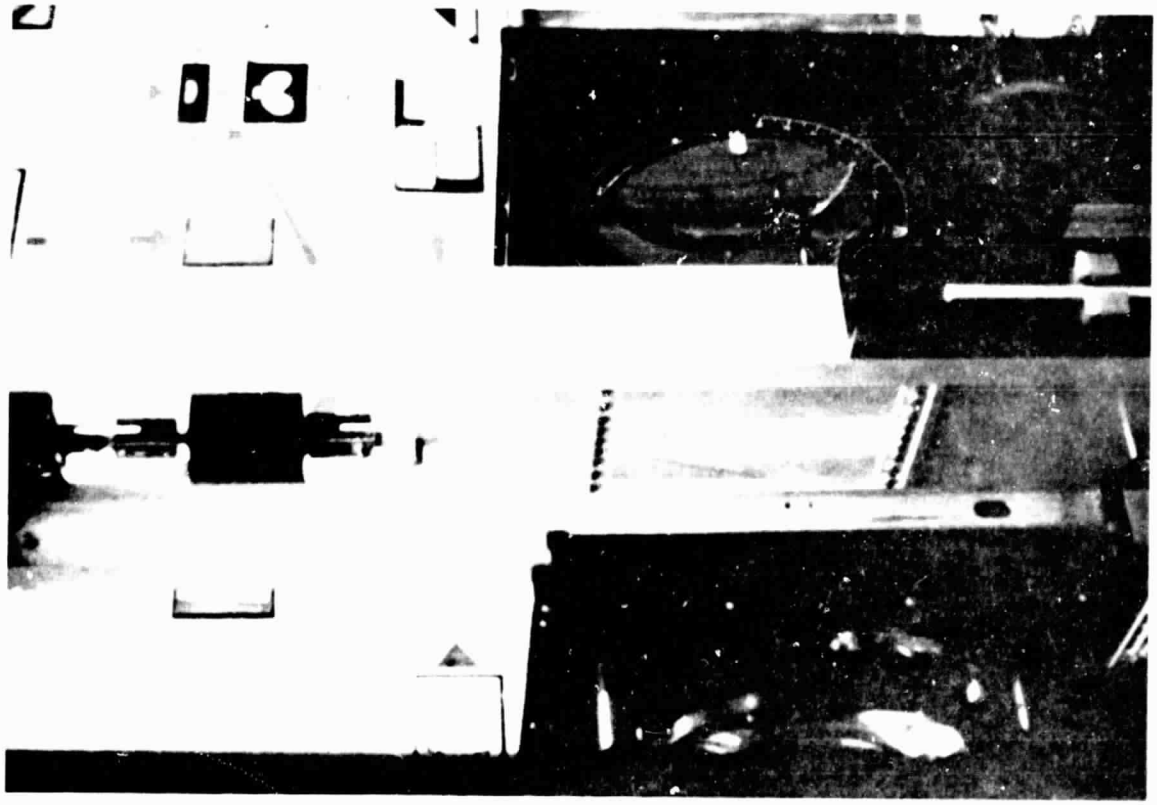

Fig. 4 - Model in Place in Polariscope

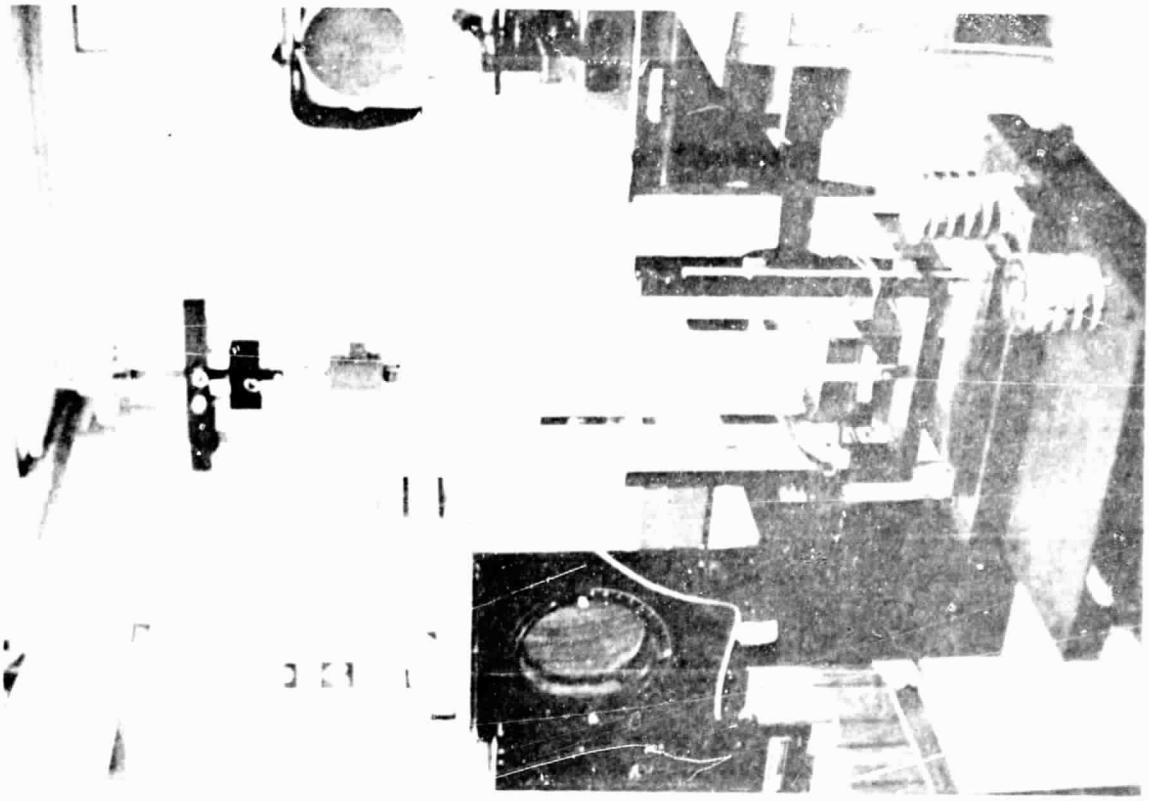

Fig. 3 - Model and Loading Frame

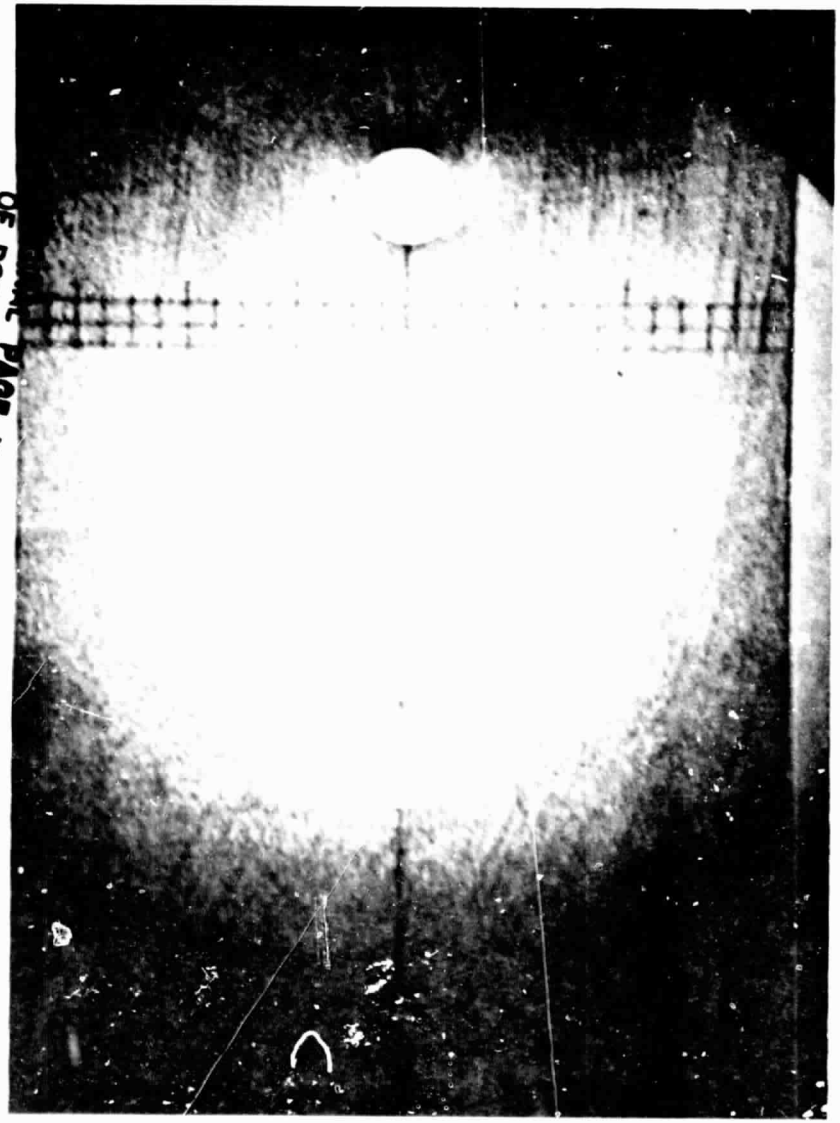

Fig. 5 - Unloaded Inner Lap as Viewed with Lightfield Circular Polariscope

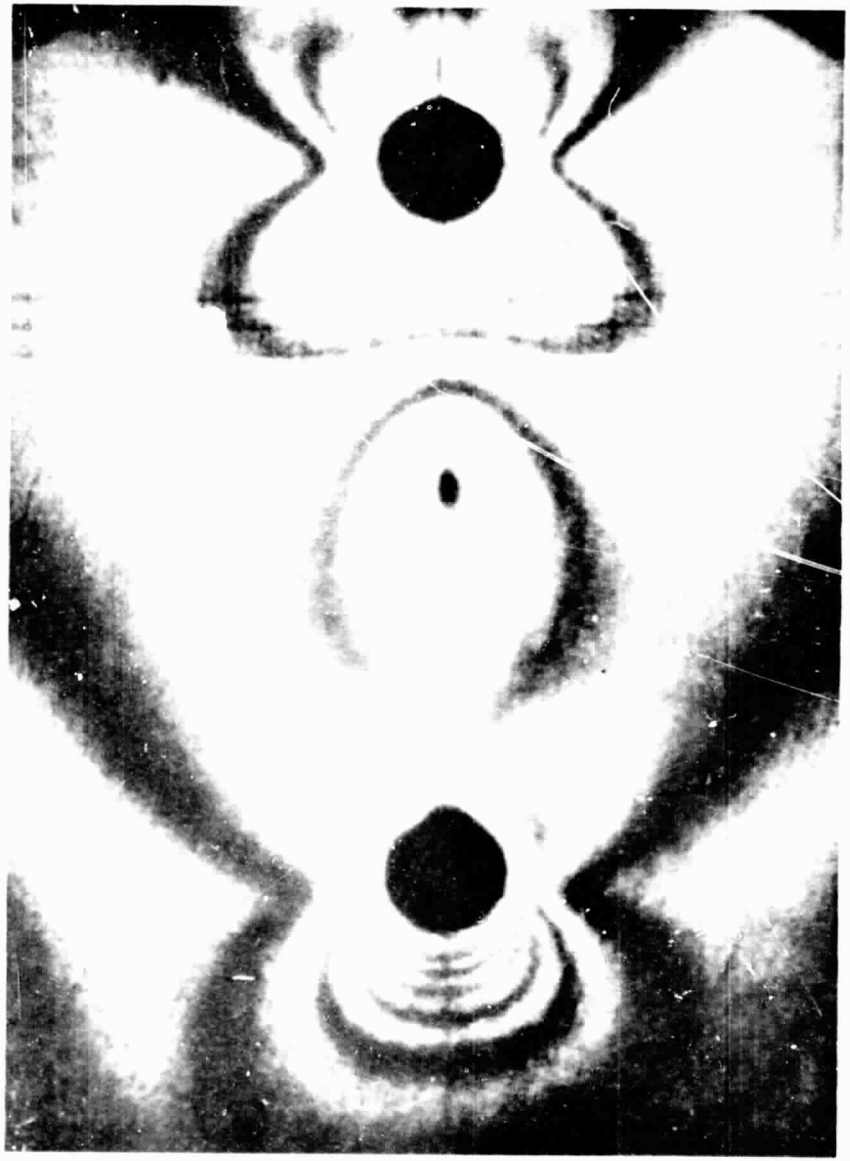

Fig. 6 - Darkfield Isochromatic Fringe Pattern, Load = 2.22 kN (500 lb.)

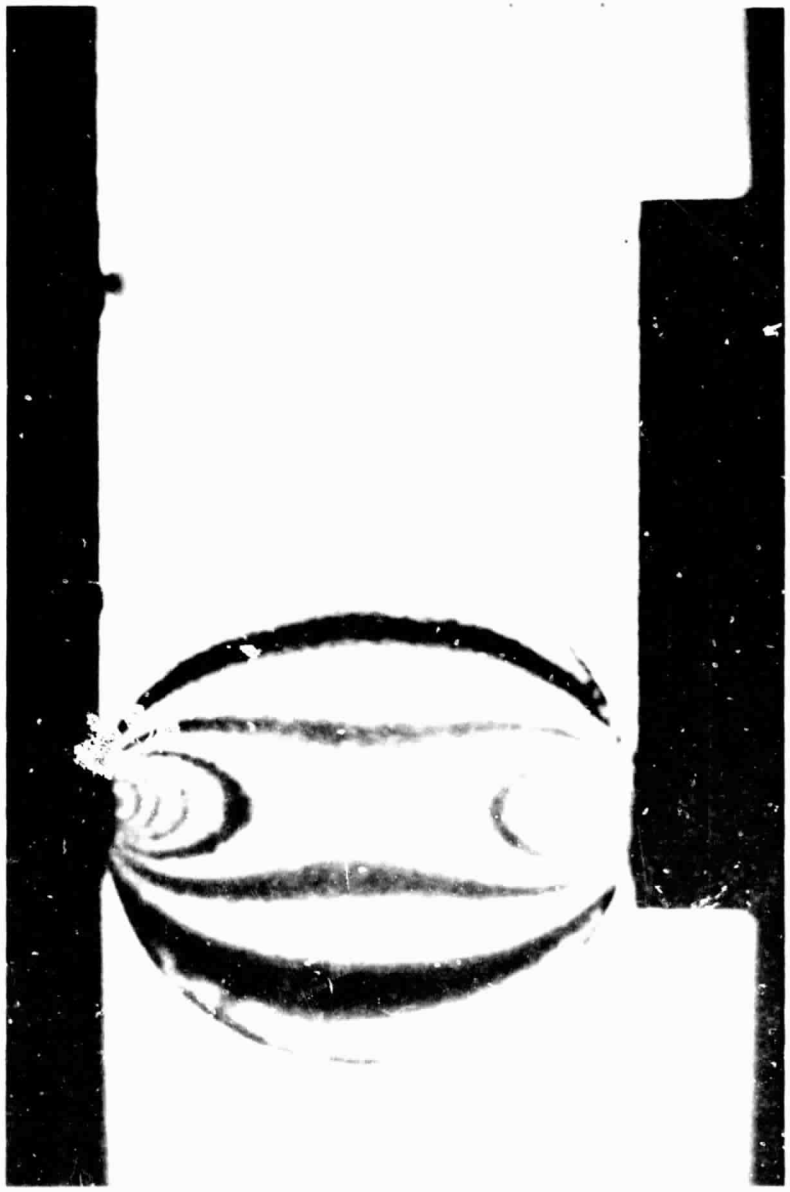

Fig. 7 - Isochromatic Fringe Patterns of PSM-1 (bottom) and Acrylite (top) Disks Subjected to Identical Compressive Loads

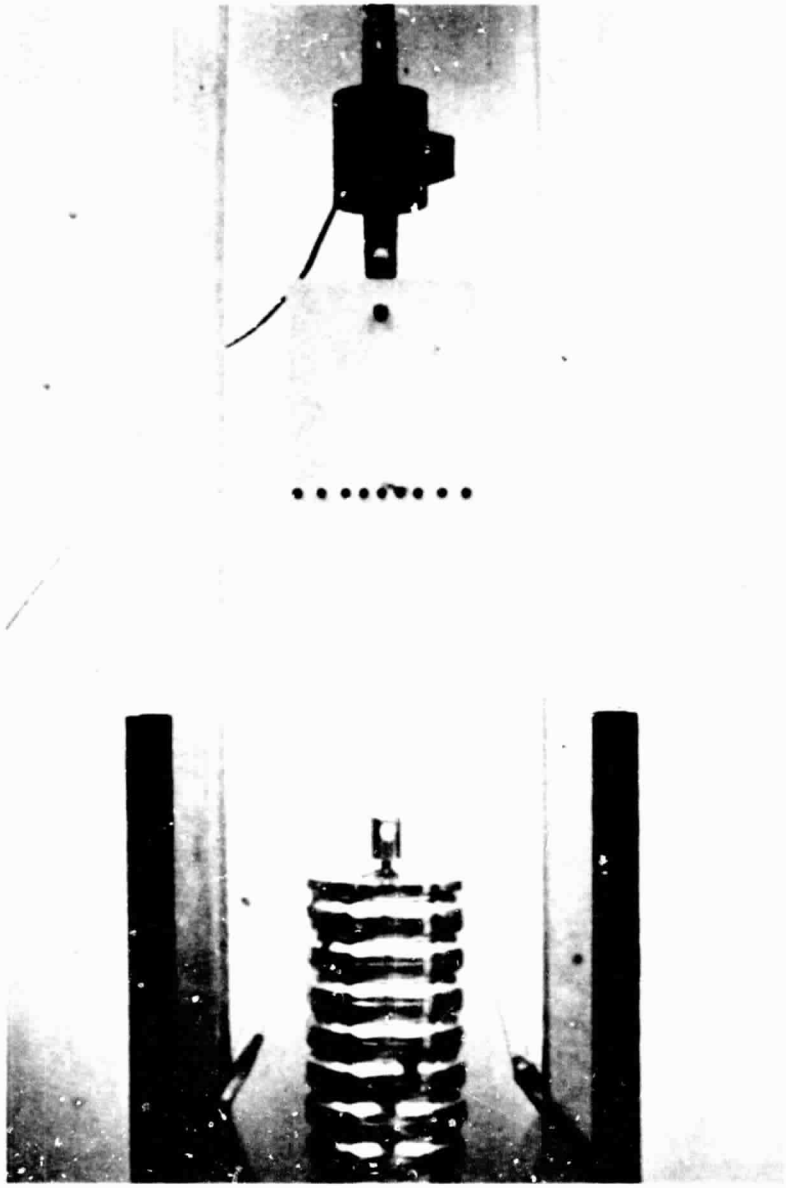

Fig. 8 - Arrangement for Loading Each Hole Independently

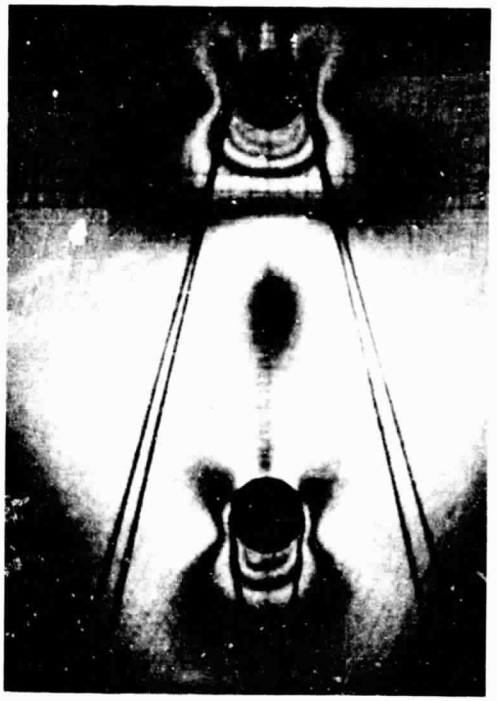

a) P_1=60%, P_2=40%

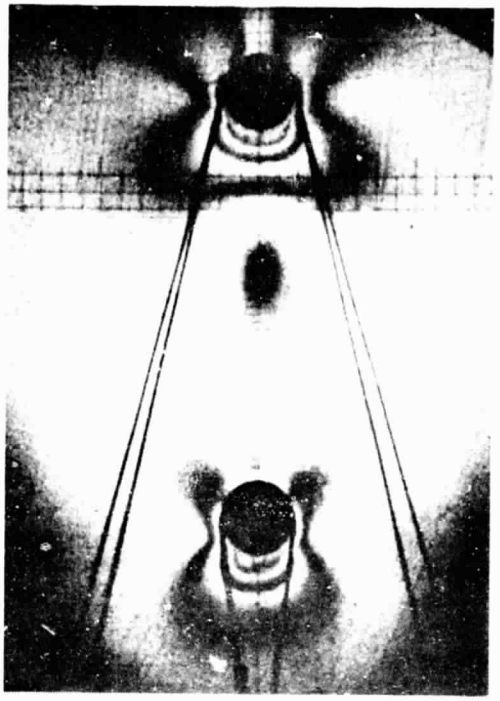

b) P_1=49%, P_2=51%

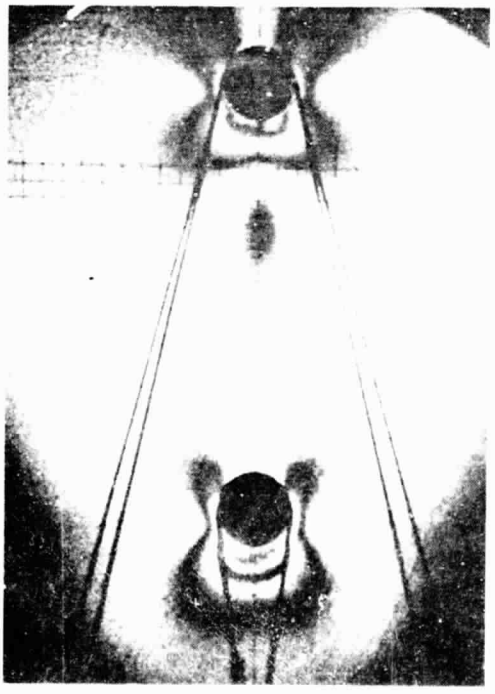

c) P_1=37%, P_2=63%

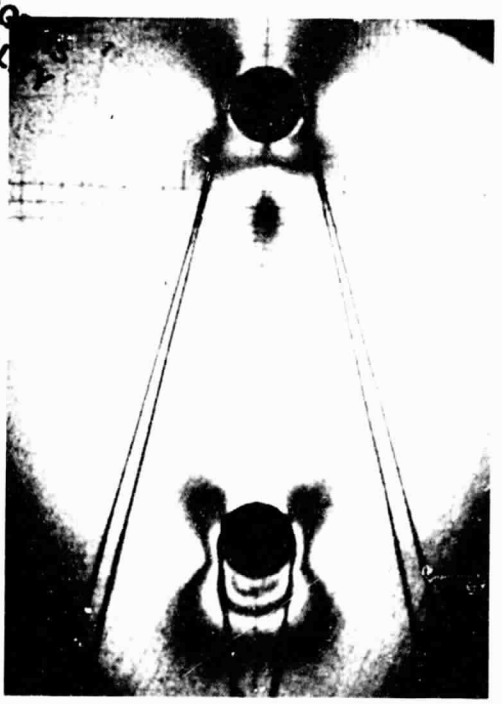

d) P_1=23%, P_2=77%

Fig. 9 - Dependence of Isotropic Point Location on Percentage of Load Reacted by Each Hole (P_1=top hole, P_2=bottom hole)

case 1: T = 749N (168 lb.), P_1 variable
dowels: A top, B bottom
case 2: P_1 = 311 N (70 lb.), T variable
dowels: A top, B bottom
case 3: P_1 = 400 N (90 lb.), T variable
dowels: B top, A bottom
case 4: P_1 = 400 N (90 lb.), T variable
dowels: A top, B bottom

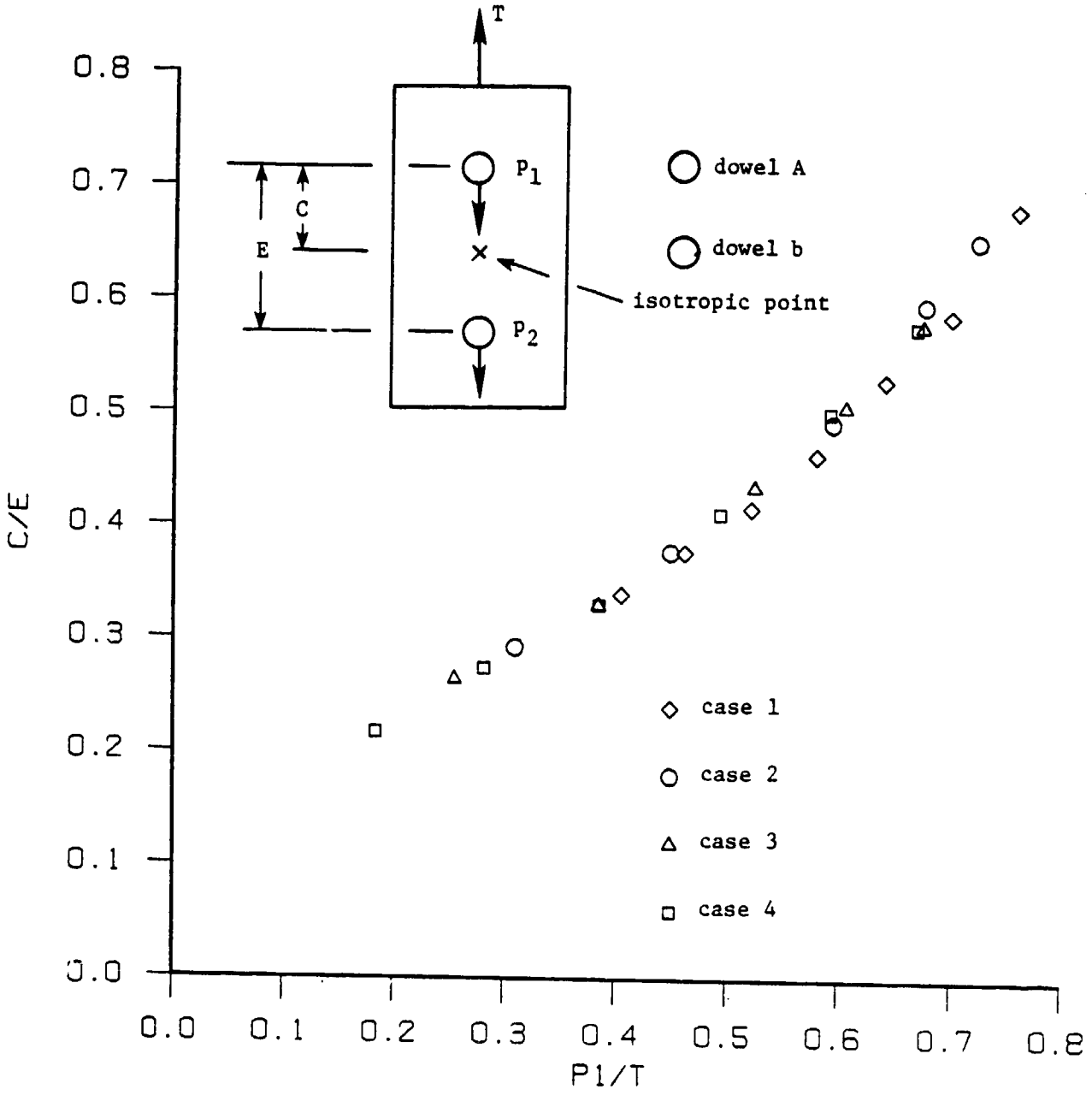

Fig. 10 - Isotropic Point Location as a Function of Load Reacted by the Lead Bolt.

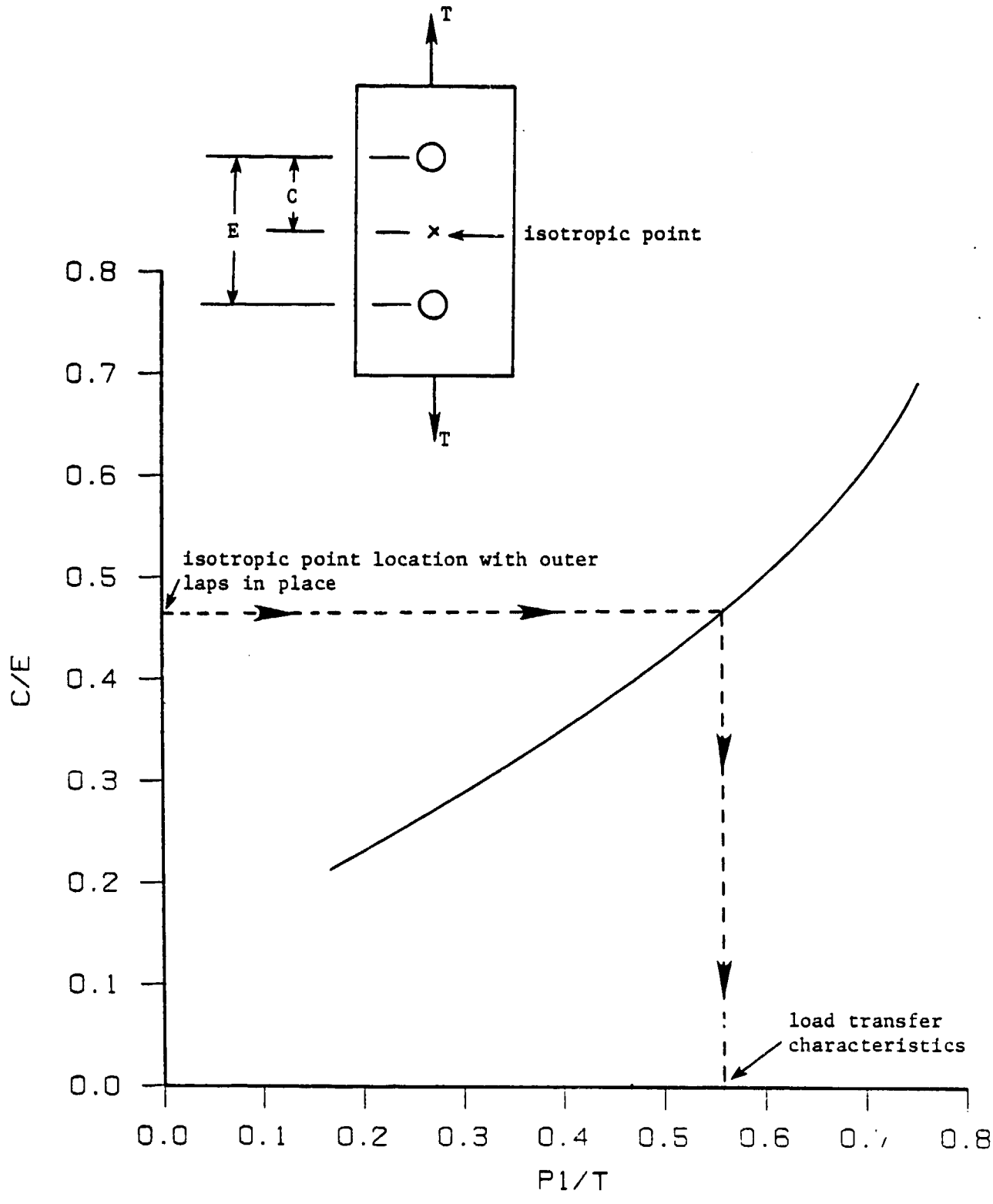

Fig. 11 - Determination of the Percentage of Load Reacted by Load Bolt, Knowing Isotropic Point Location

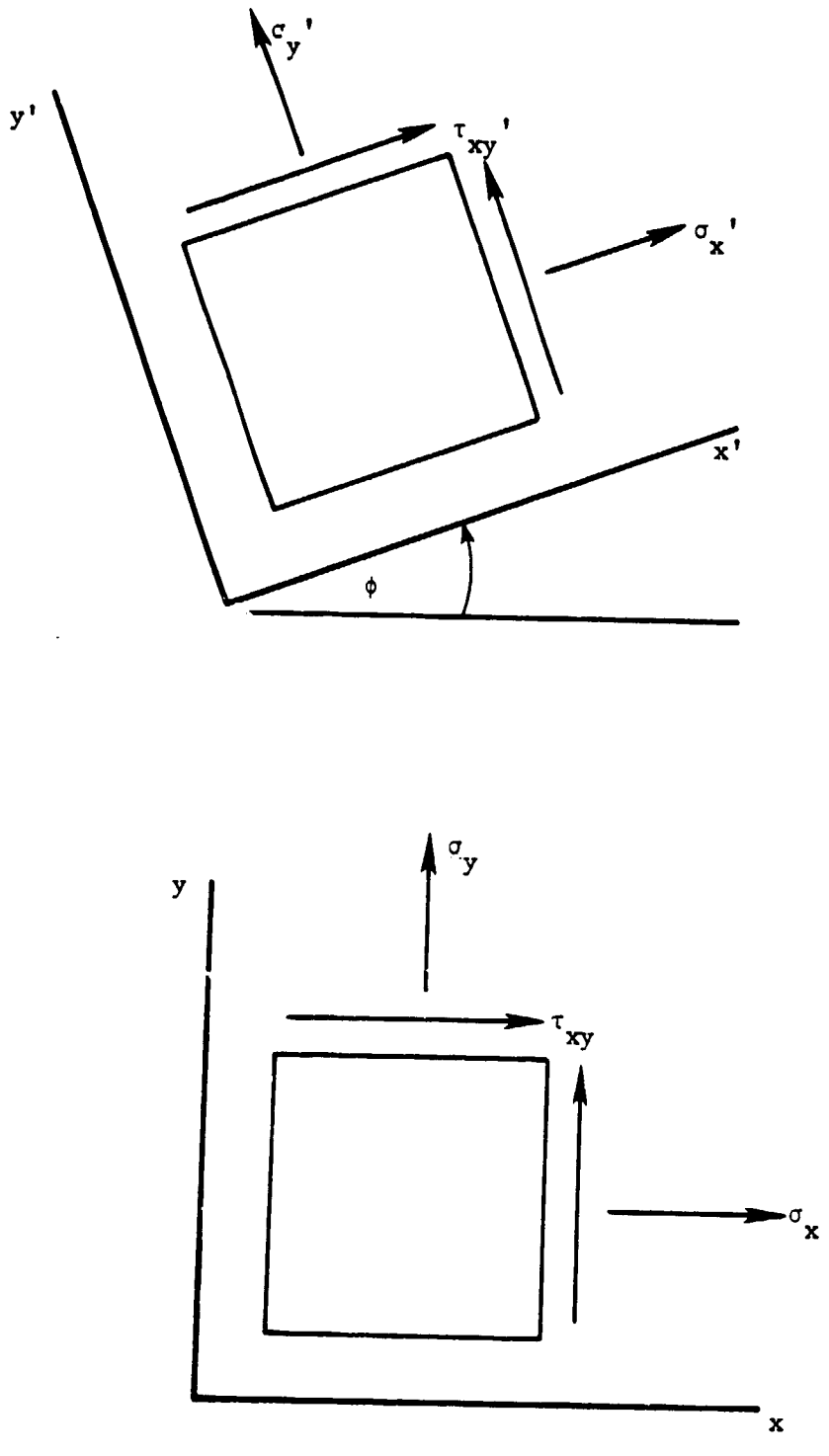

Fig. 12 - Transformation of Stresses

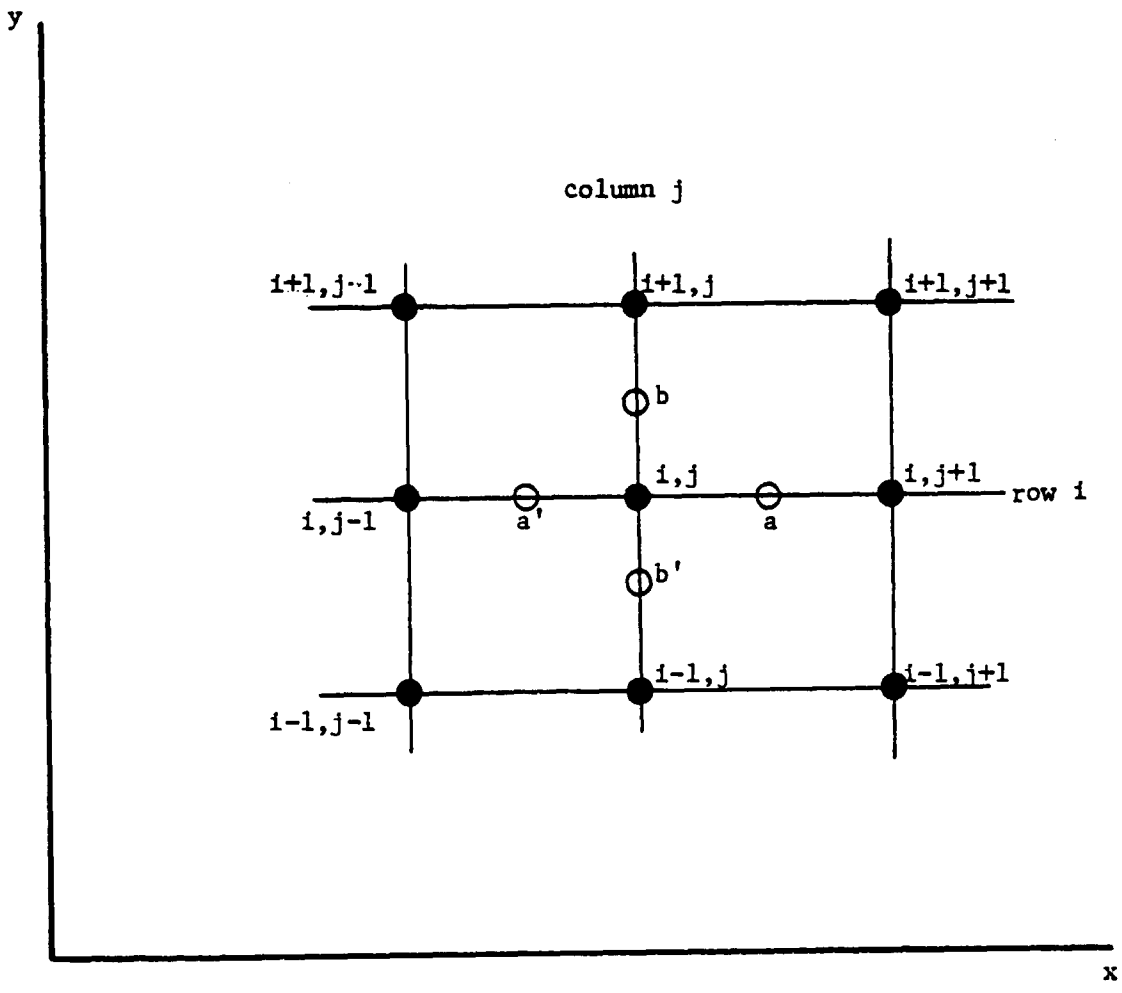

Fig. 13 - Finite-Difference Grid System

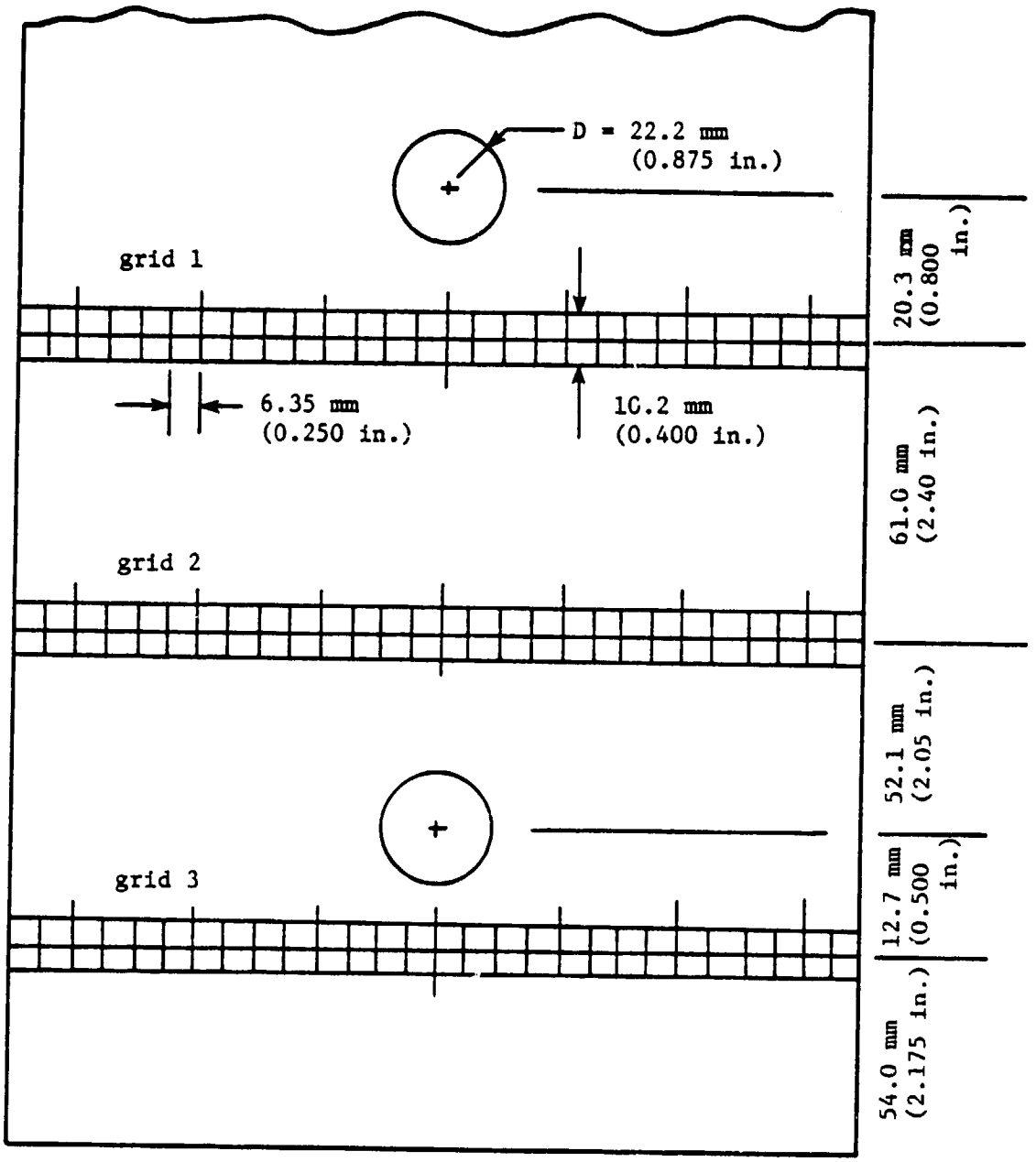

Fig. 14 - Locations of Grid Systems on Model

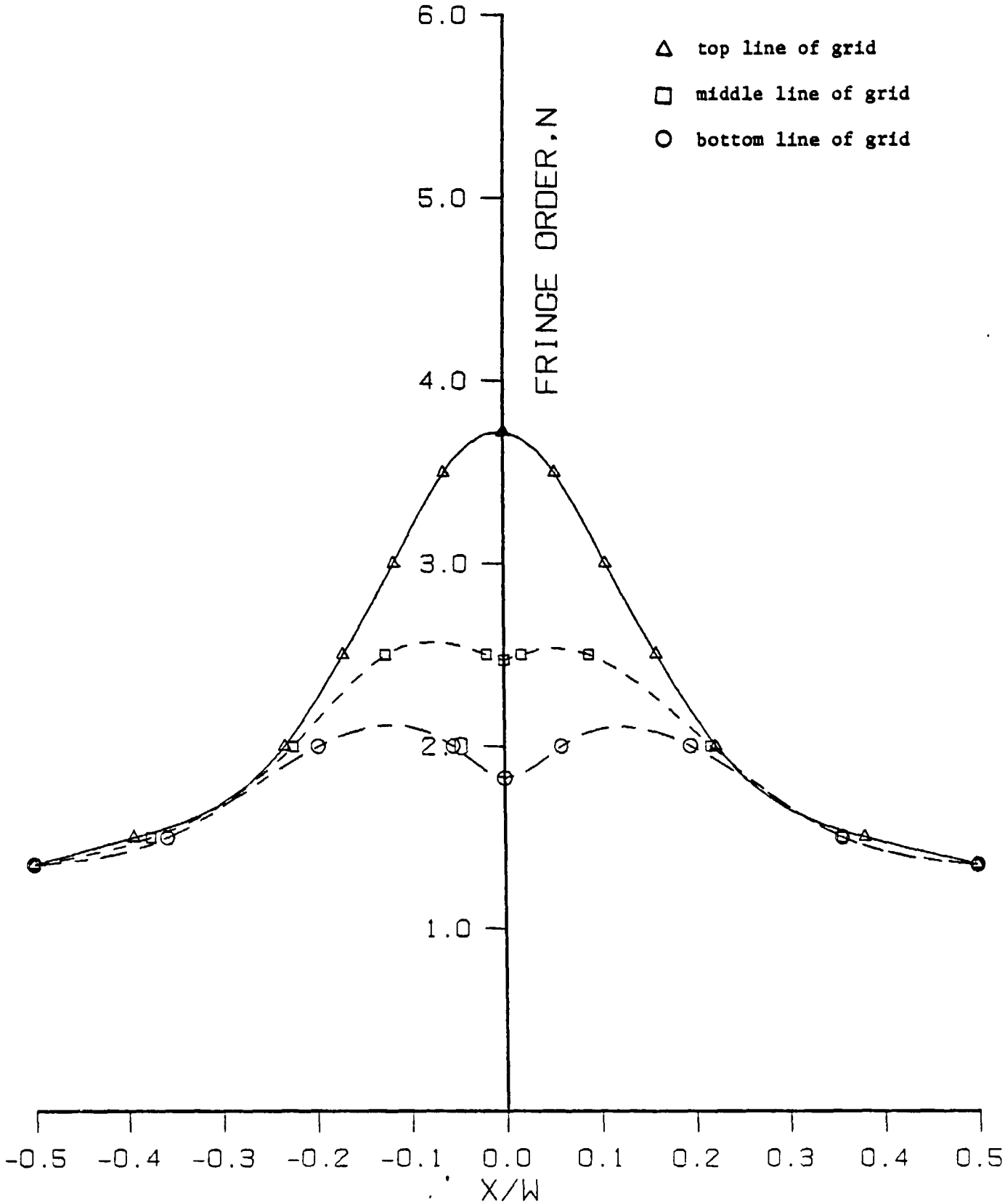

Fig. 15 - Isochromatic Fringe Order for Grid 1, Load = 2.2 kN (500 lb.), c = 103 MPa/fringe (150 psi/fringe)

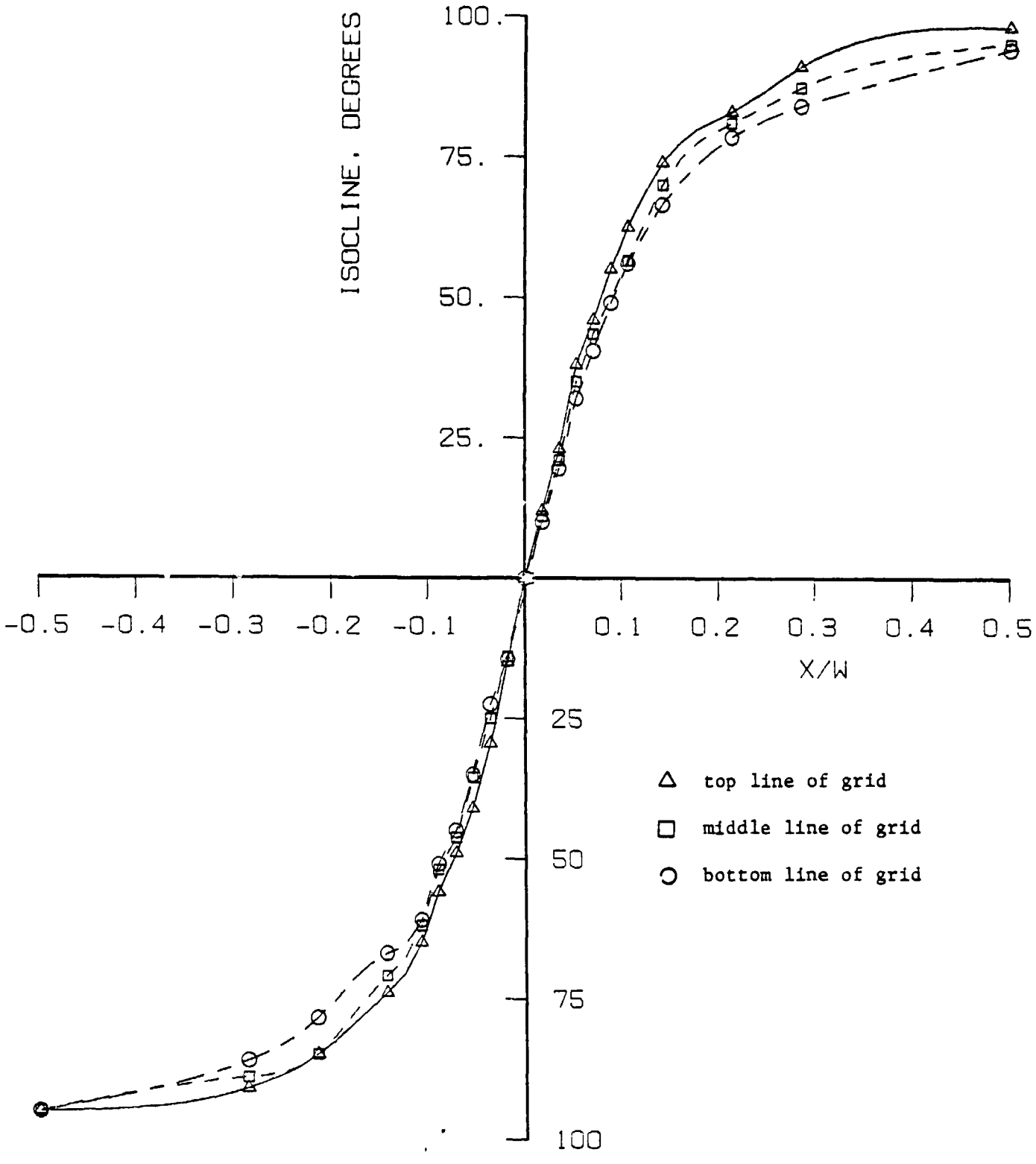

Fig. 16 - Isoclinic Angle for Grid 1

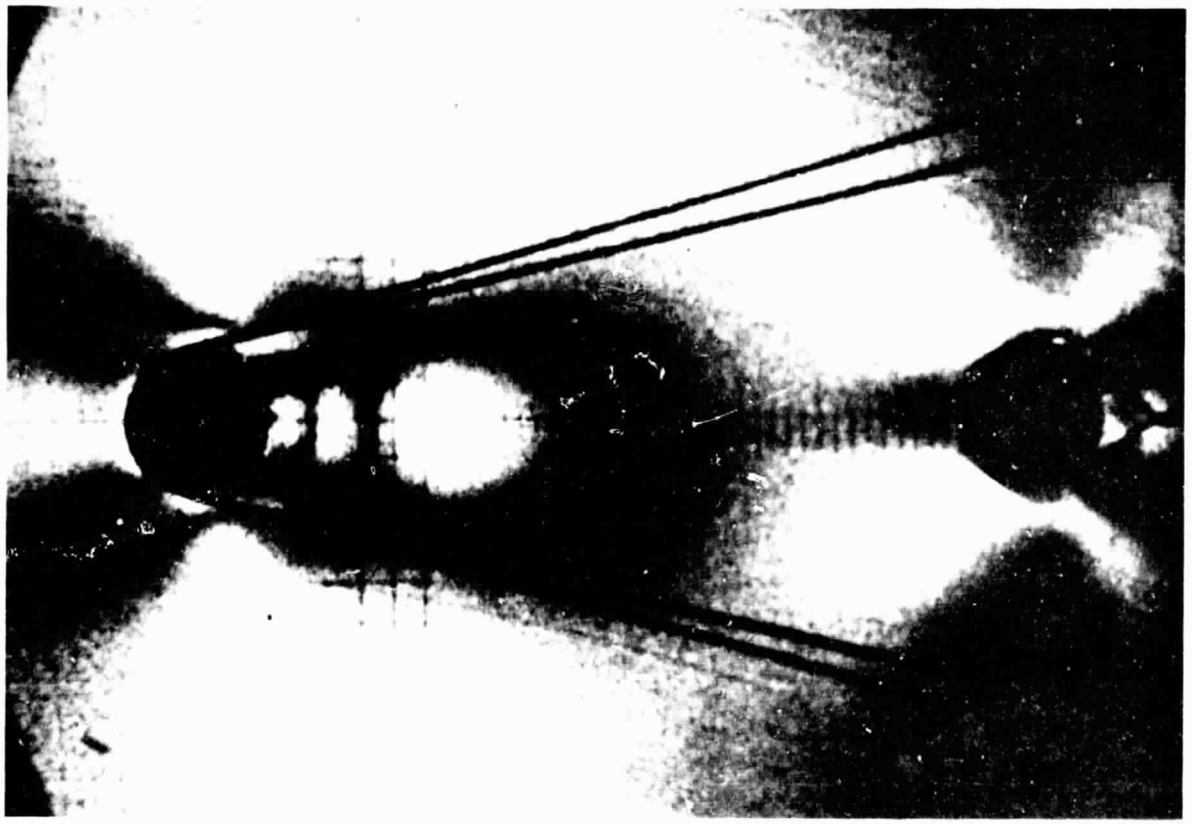

Fig. 18 - The 45° Isocline Fringe

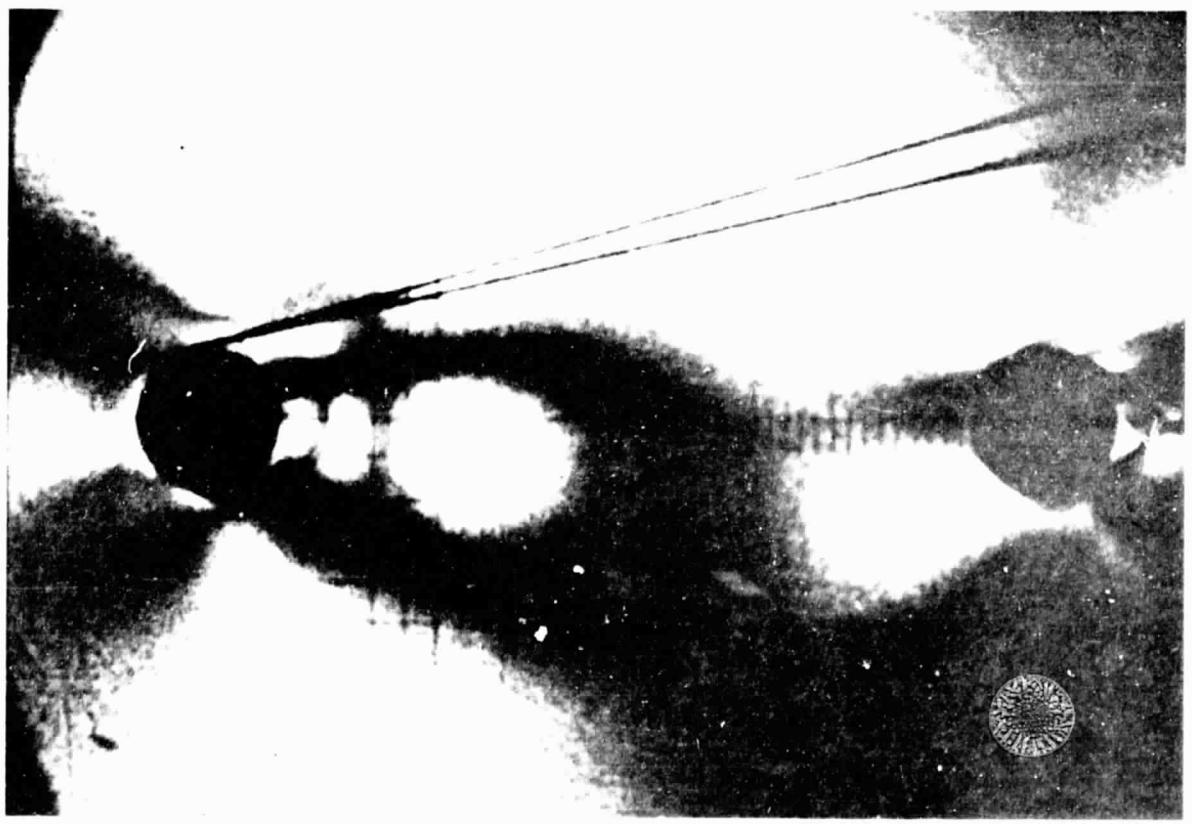

Fig. 17 - The 30° Isocline Fringe

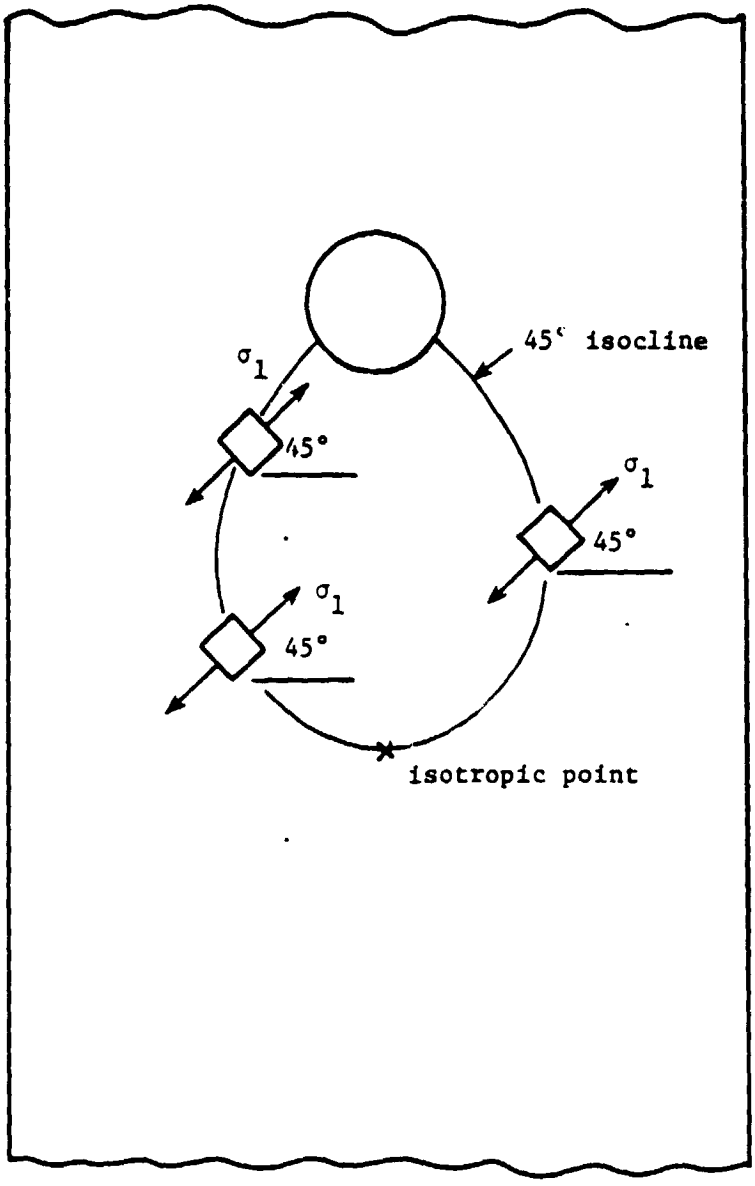

Fig. 19 - Physical Meaning of an Isoclinic Fringe
(θ = 45°)

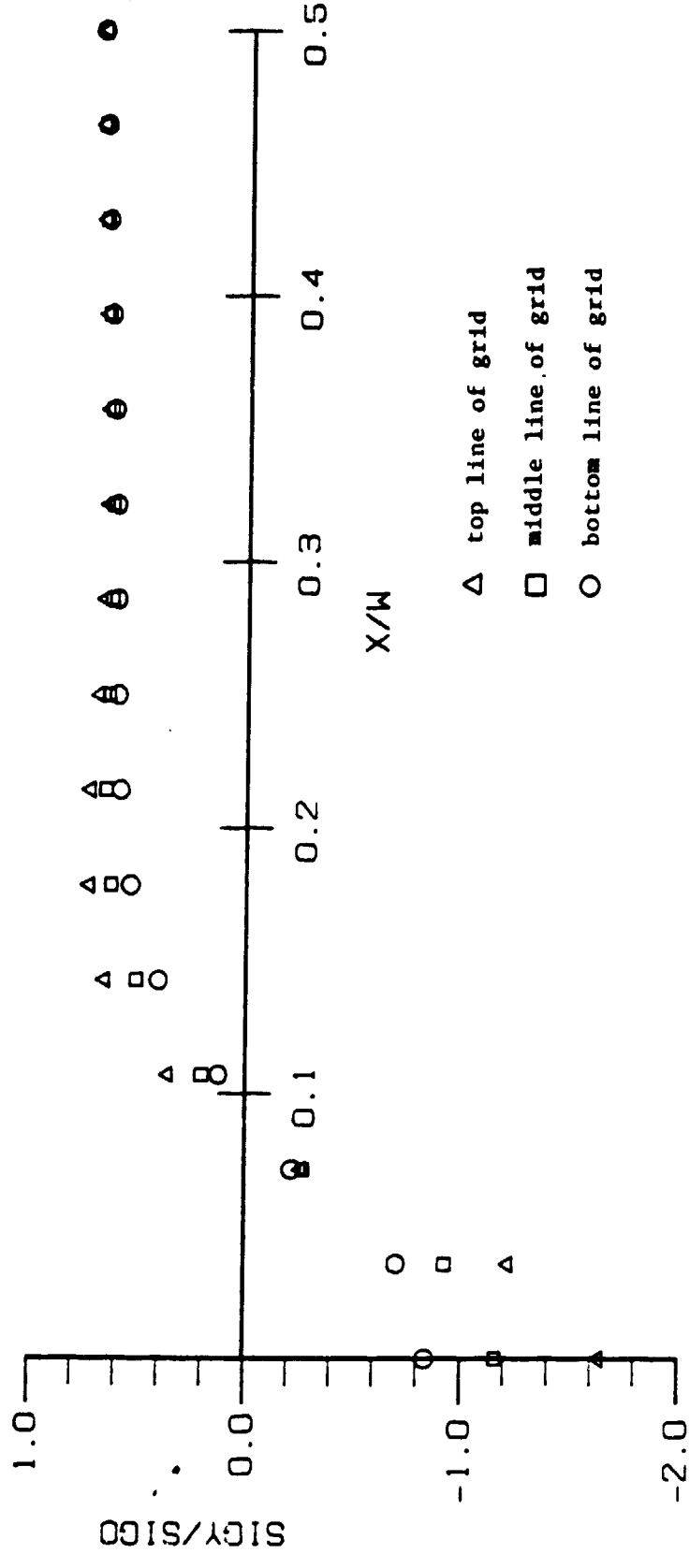

Fig. 20 - Variation of σ_y with Width, Grid 1

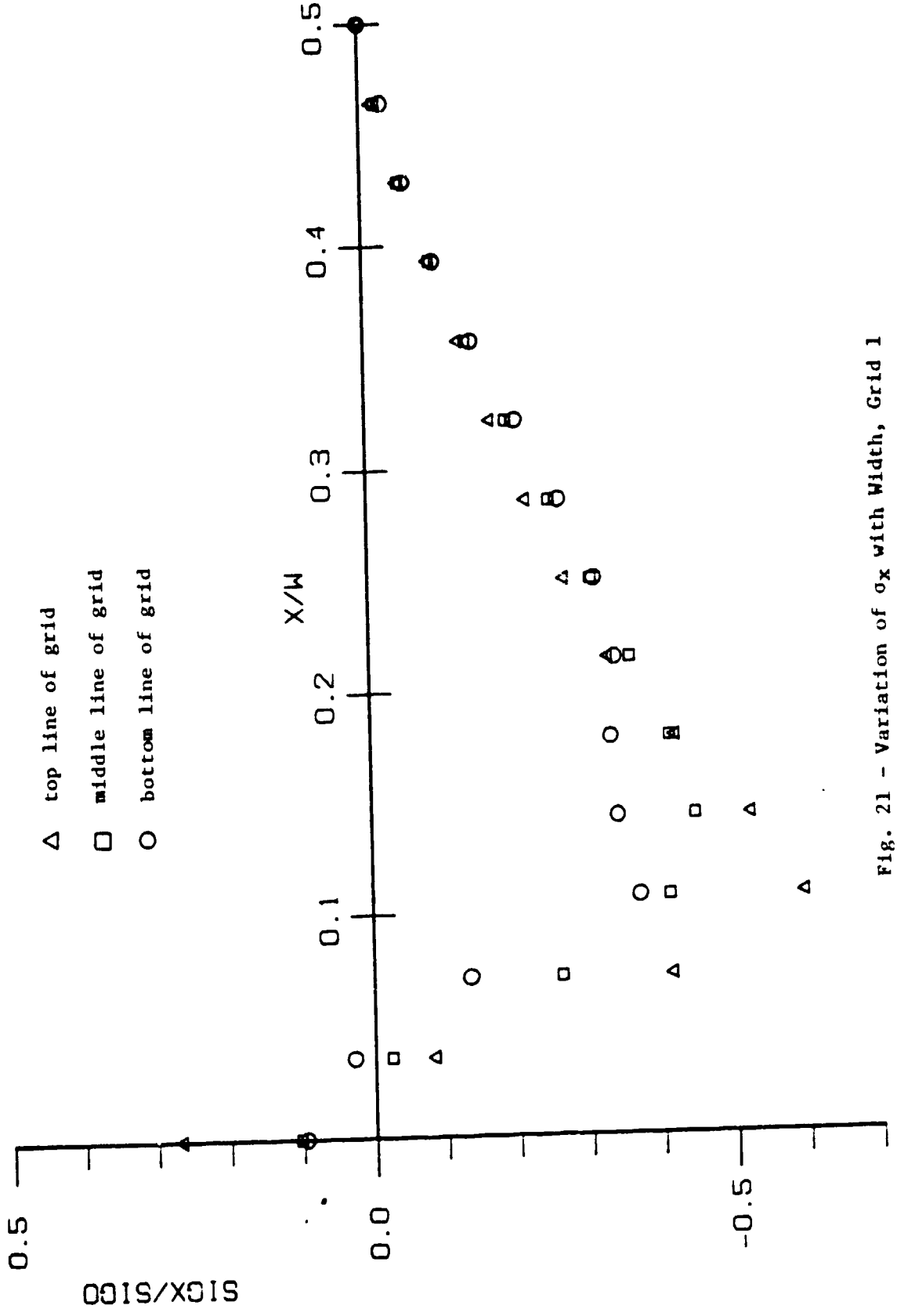

Fig. 21 - Variation of σ_x with Width, Grid 1

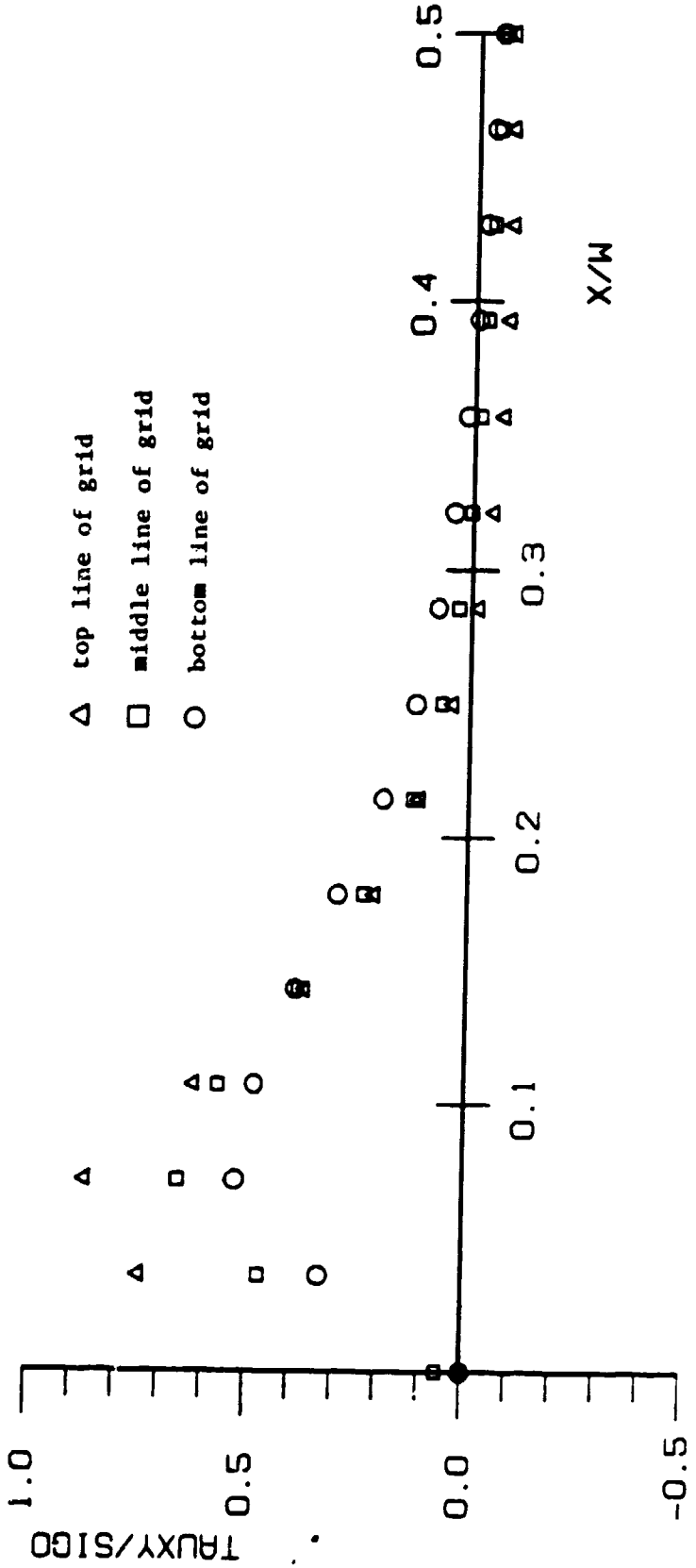

Fig. 22 - Variation of τ_{xy} with Width, Grid 1

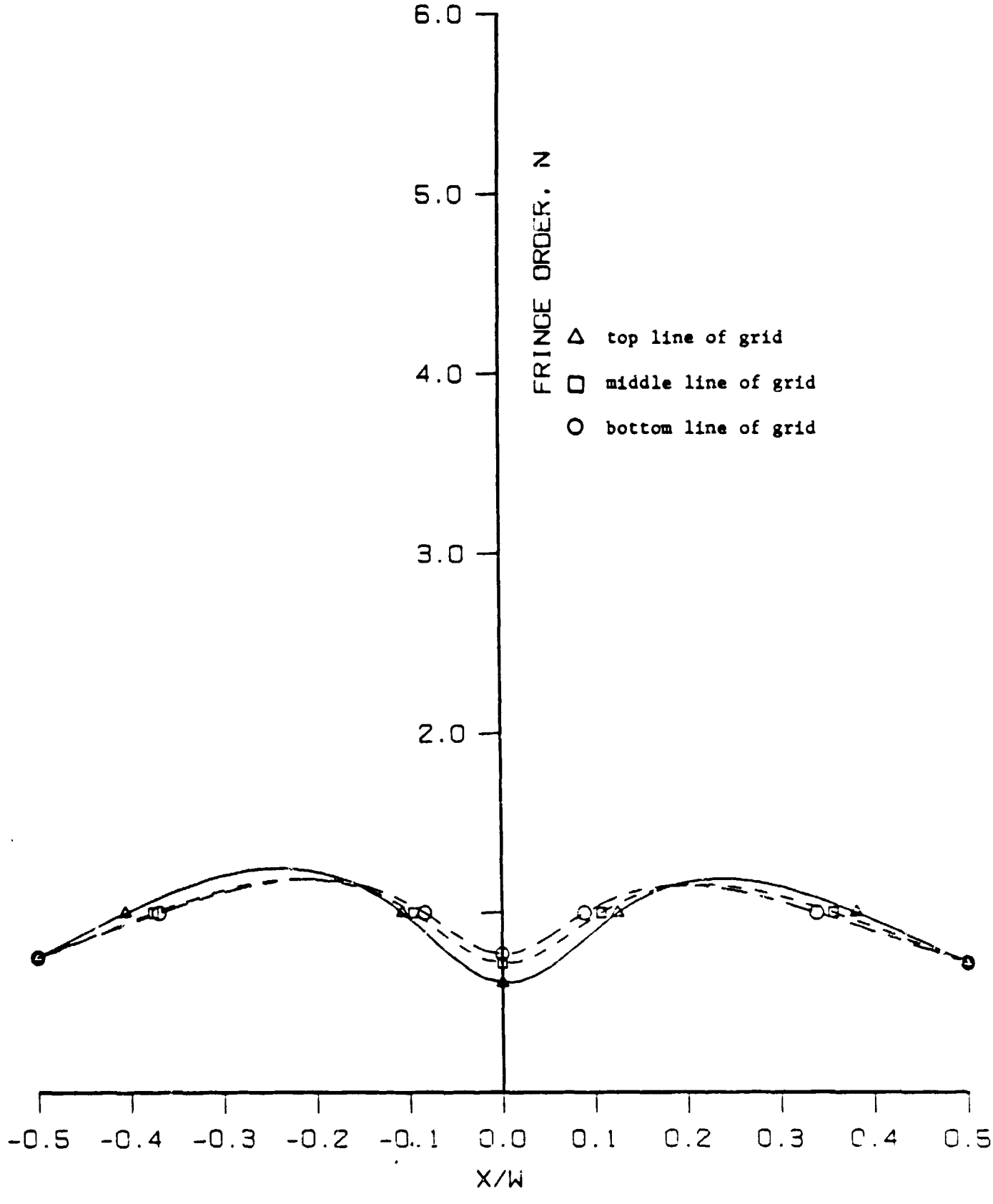

Fig. 23 - Isochromatic Fringe Order for Grid 2, Load = 2.2 kN (500 lb.), c = 1.03 MPa/fringe (150 psi/fringe)

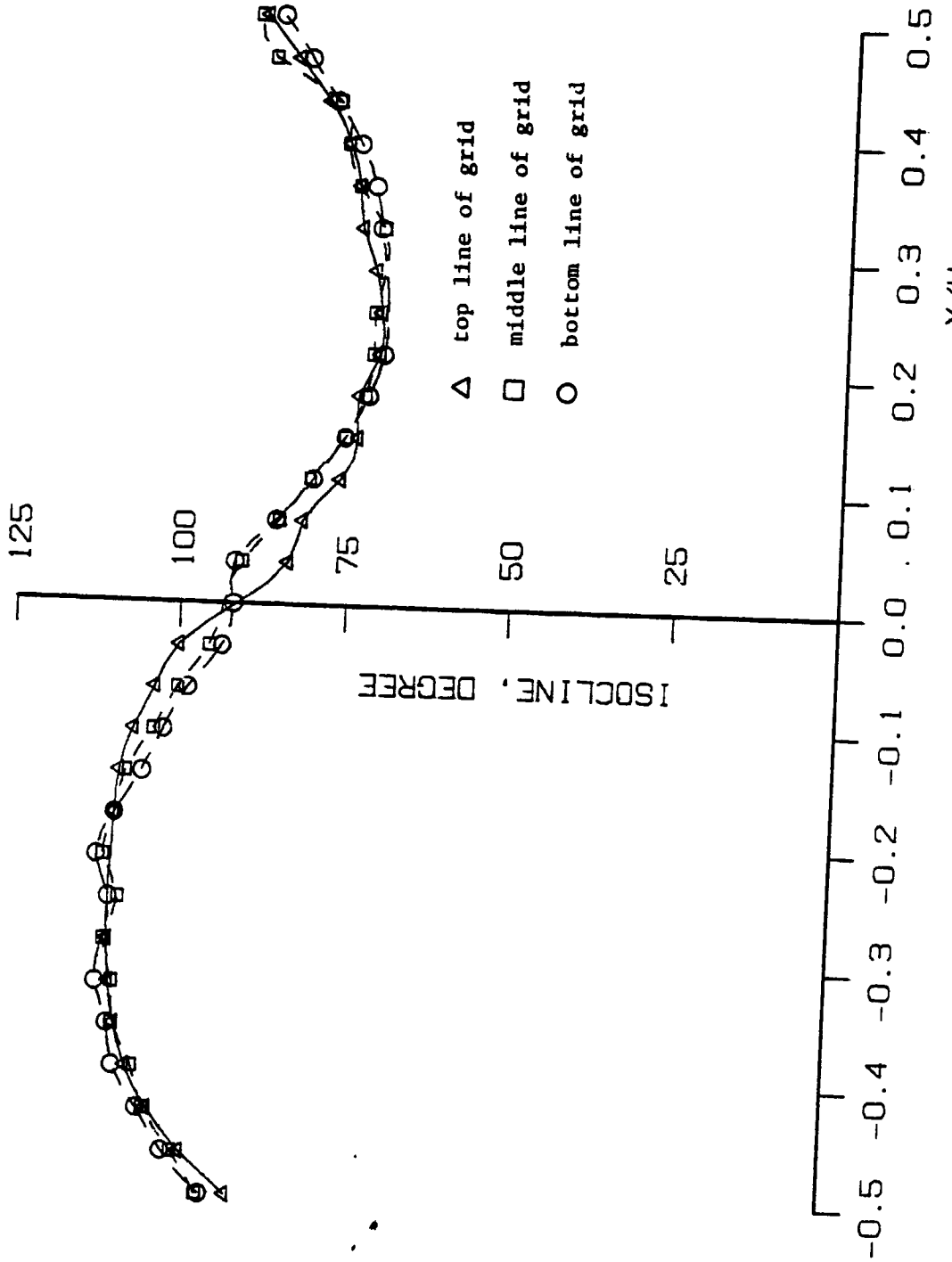

Fig. 24 - Isoclinic Angle for Grid 2

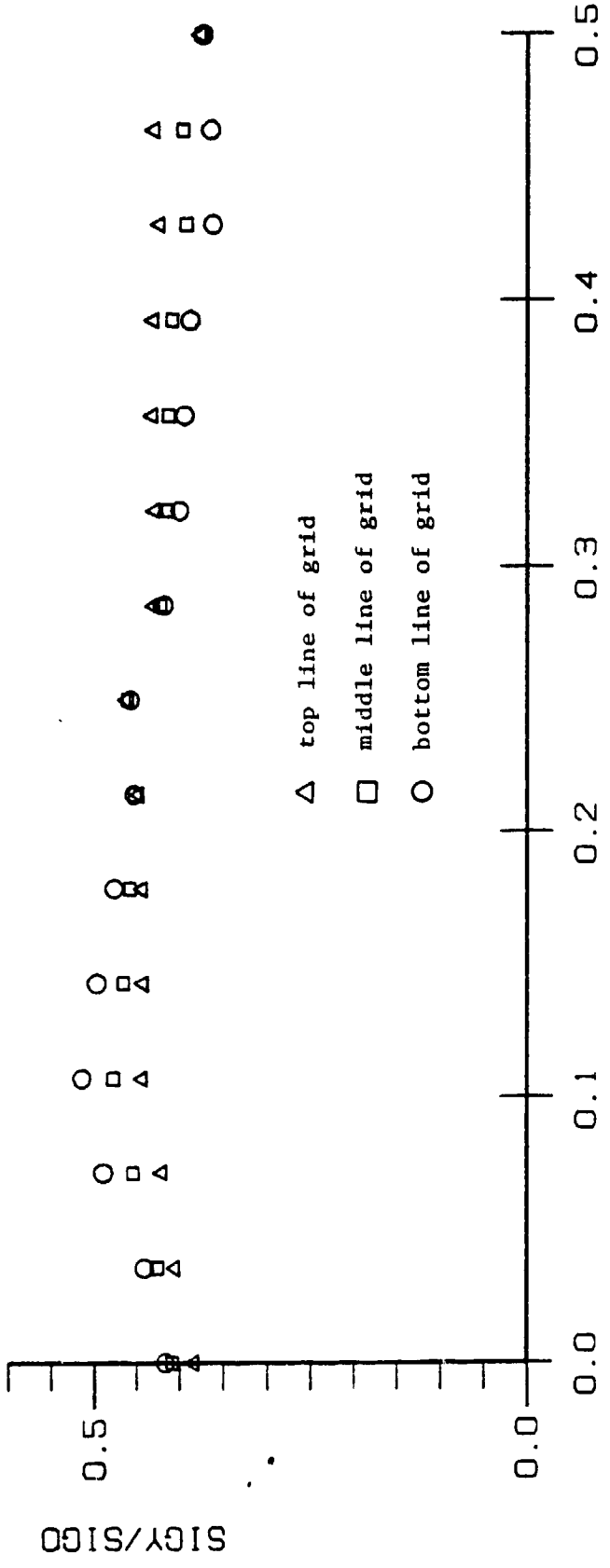

Fig. 25 - Variation of σ_y with Width, Grid 2

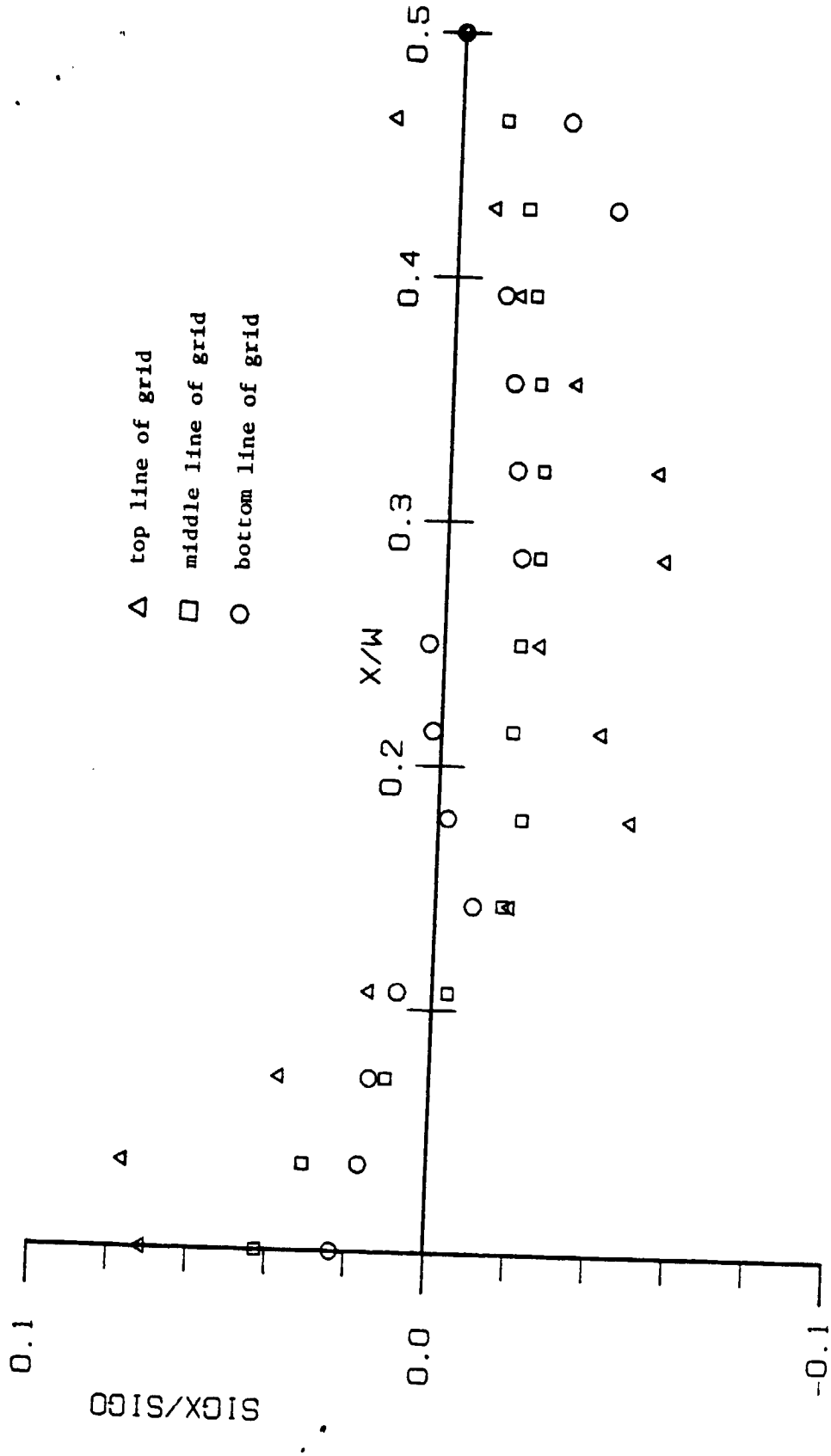

Fig. 26 - Variation of σ_x with Width, Grid 2

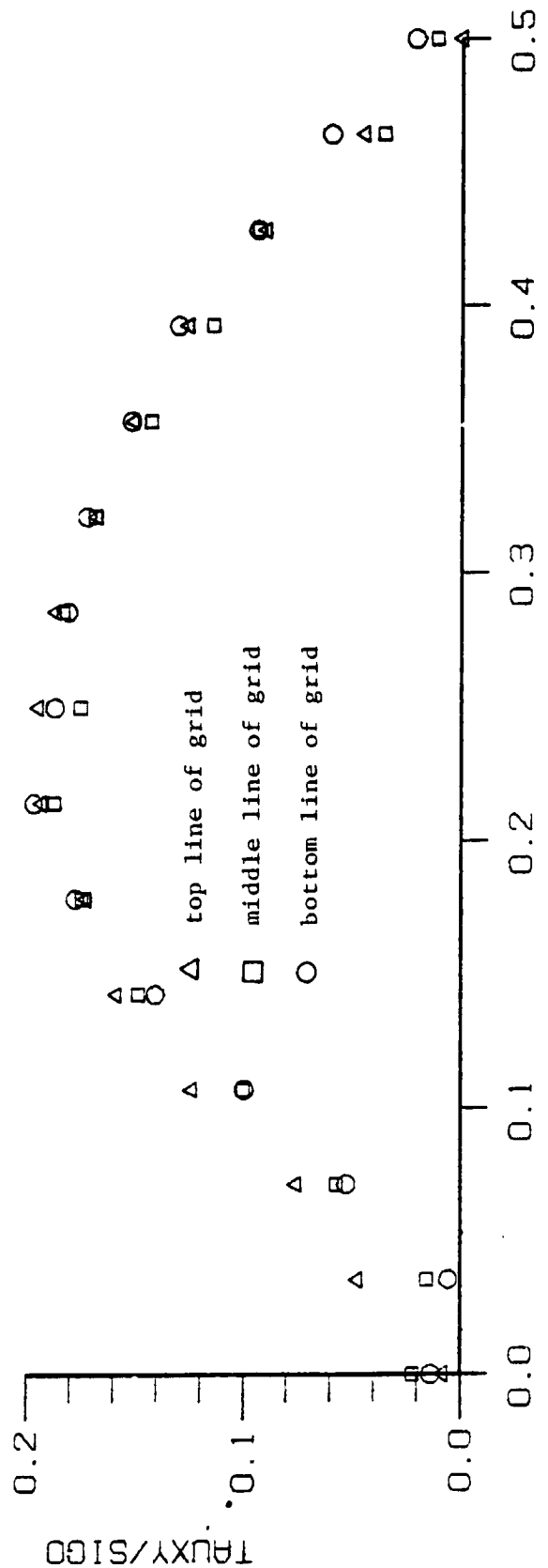

Fig. 27 - Variation of τ_{xy} with Width, Grid 2

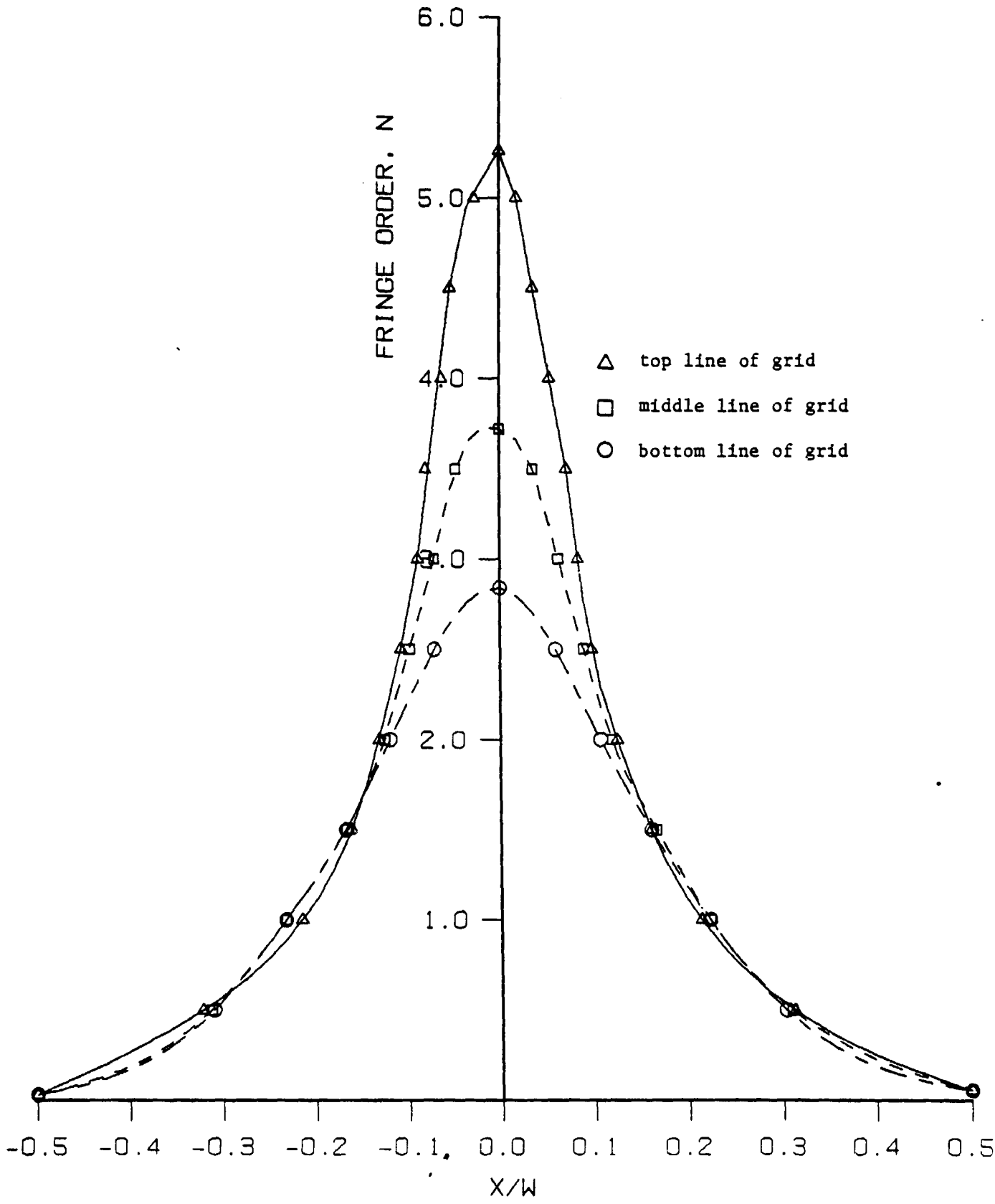

Fig. 28 - Isochromatic Fringe Order for Grid 3, Load = 2.2 kN (500 lb.) c = 1.03 MPa/fringe (150 psi/fringe)

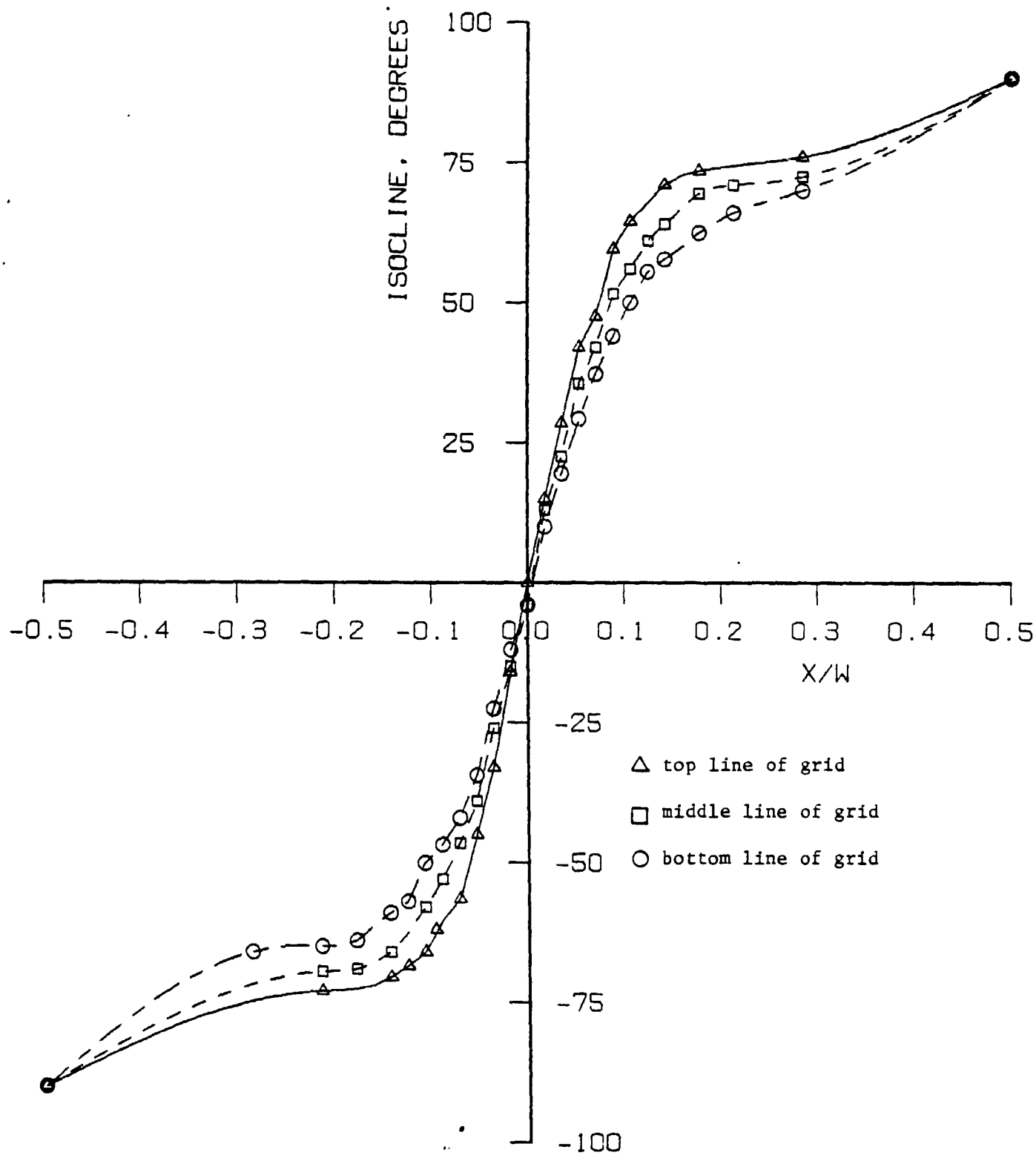

Fig. 29 - Isoclinic Angle for Grid 3

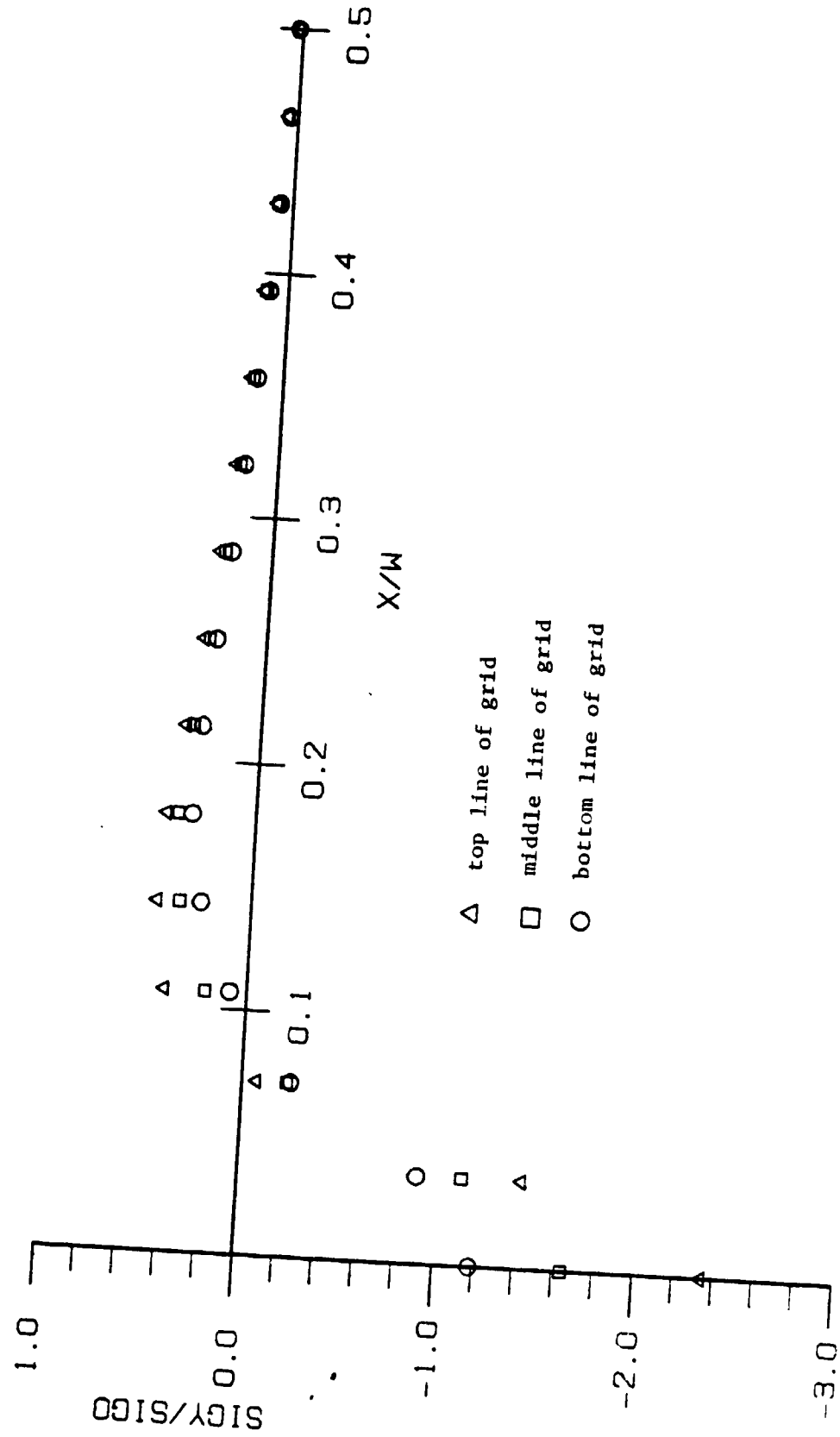

Fig. 30 - Variation of σ_y with Width, Grid 3

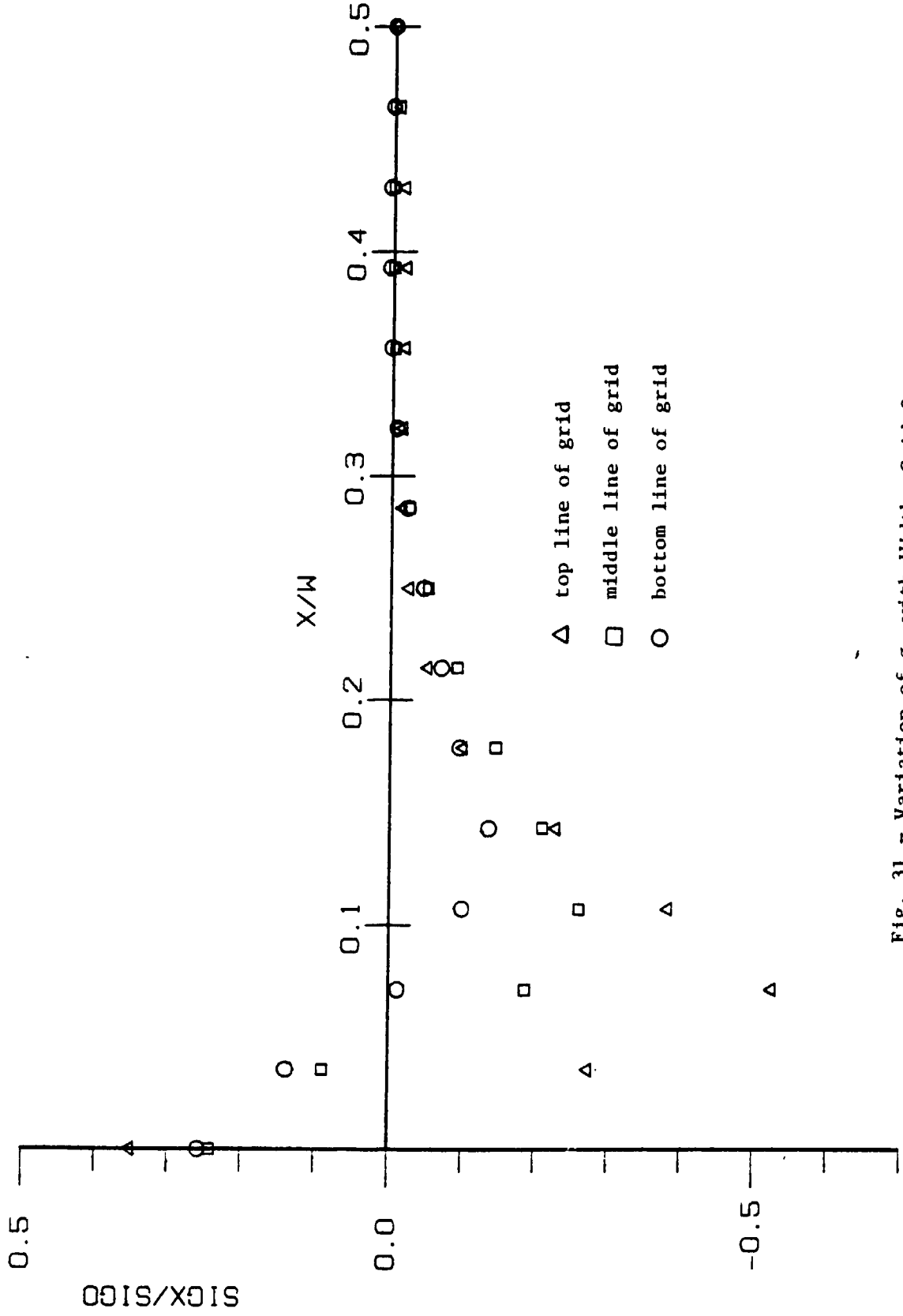

Fig. 31 - Variation of σ_x with Width, Grid 3

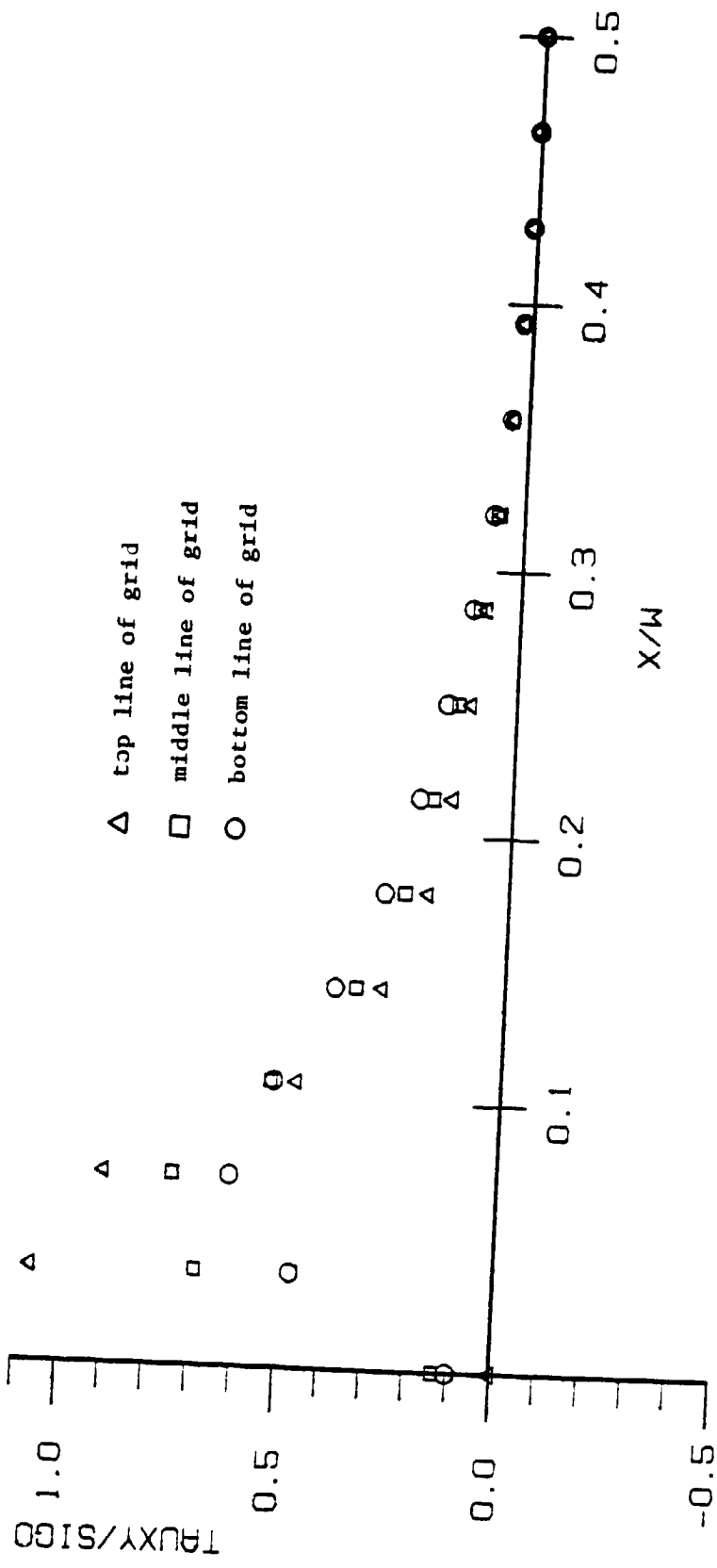

Fig. 32 - Variation of τ_{xy} with Width, Grid 3